

NASA Contractor Report 187089

3356  
P-132

# A Modal Aeroelastic Analysis Scheme for Turbomachinery Blading

(NASA-CR-187089) A MODAL AEROELASTIC  
ANALYSIS SCHEME FOR TURBOMACHINERY BLADING  
M.S. Thesis - Case Western Reserve Univ.  
Final Report (Sverdrup Technology) 132 p

N91-21138

Unclas  
CSCL 21E G3/07 0003556

Todd E. Smith  
*Sverdrup Technology, Inc.*  
*Lewis Research Center Group*  
*Brook Park, Ohio*

March 1991

Prepared for  
Lewis Research Center  
Under Contract NAS3-25266

**NASA**  
National Aeronautics and  
Space Administration



A MODAL AEROELASTIC ANALYSIS SCHEME  
FOR TURBOMACHINERY BLADING

Todd E. Smith  
Sverdrup Technology, Inc.  
Lewis Research Center Group  
Brook Park, Ohio 44142

ABSTRACT

An aeroelastic analysis is developed which has general application to all types of axial-flow turbomachinery blades. The approach is based on linear modal analysis, where the blade's dynamic response is represented as a linear combination of contributions from each of its in-vacuum free vibrational modes. A compressible linearized unsteady potential theory is used to model the flow over the oscillating blades. The two-dimensional unsteady flow is evaluated along several stacked axisymmetric strips along the span of the airfoil. The unsteady pressures at the blade surface are integrated to result in the generalized force acting on the blade due to simple harmonic motions. The unsteady aerodynamic forces are coupled to the blade normal modes in the frequency domain using modal analysis. An iterative eigenvalue problem is solved to determine the stability of the blade when the unsteady aerodynamic forces are included in the analysis. The approach is demonstrated by applying it to a high-energy subsonic turbine blade from a rocket engine turbopump power turbine. The results indicate that this turbine could undergo flutter in an edgewise mode of vibration.

## ACKNOWLEDGEMENTS

I wish to thank my employer, Sverdrup Technology, Inc. for its continued support and encouragement during the course of my graduate study. In addition, I also would like to thank the NASA Lewis Research Center (LeRC), in particular George Stefko and Oral Mehmed, for their sponsorship of this research activity.

On a personal note, I would like to thank Dr. Robert Kielb of General Electric Corp. for introducing me to the field of aeroelasticity. I would also like to express my warm regards to my friend Dr. Durbha Murthy, a resident research associate at NASA LeRC, for the many hours of thoughtful discussions we shared over several years.

## TABLE OF CONTENTS

ACKNOWLEDGEMENTS .....	ii
LIST OF FIGURES .....	vii
LIST OF TABLES .....	ix
NOMENCLATURE .....	x
CHAPTER 1 - INTRODUCTION .....	1
1.1 Introduction .....	1
1.2 Literature Review .....	4
1.21 Turbomachinery Aeroelastic Problems .....	5
1.22 Unsteady Aerodynamic Models .....	9
1.23 Aeroelastic Analysis Models .....	16
1.3 Objective of Current Work .....	22
CHAPTER 2 - ANALYTICAL DEVELOPMENT .....	24
2.1 Aerodynamic Analysis .....	24
2.11 Steady Full Potential Flow .....	25
2.12 Linearized Unsteady Potential Flow .....	28
2.2 Structural Dynamic Analysis .....	33
2.3 Aeroelastic Model .....	38

CHAPTER 3 - APPLICATION OF METHOD .....	48
3.1 Computer Program .....	48
3.2 SSME HPOTP Turbine Description .....	49
3.3 Aeroelastic Model .....	52
3.4 Structural Dynamic Results .....	54
3.5 Aerodynamic Results .....	56
3.51 Steady Aerodynamic Results .....	58
3.52 Unsteady Aerodynamic Results .....	59
3.6 Aeroelastic Results .....	62
 CHAPTER 4 - CONCLUSION AND RECOMMENDATIONS .....	 67
4.1 Conclusion .....	67
4.2 Recommendations .....	69
 REFERENCES .....	 72
 APPENDIX A .....	 77
 TABLES .....	 88
 FIGURES .....	 90

## LIST OF FIGURES

- Figure 1. Cascade representation of rotor inlet and exit flows
- Figure 2. Cascade and airfoil geometry and nomenclature
- Figure 3. Steady solution blade-to-blade passage and boundary conditions
- Figure 4. Steady flow computational meshes, (a) global mesh, (b) local mesh
- Figure 5. Unsteady solution cascade boundary conditions
- Figure 6. Oscillating airfoil displacement vector  $\vec{r}$  definition
- Figure 7. FREPS program aeroelastic stability logic flowchart
- Figure 8. Modal aerodynamic matrix  $[A]$  logic flowchart
- Figure 9. SSME high pressure oxygen turbopump (HPOTP) cross-section
- Figure 10. SSME HPOTP turbine blade finite element model
- Figure 11. Turbine blade aeroelastic strip definitions
- Figure 12. Turbine blade airfoil description at 75% span
- Figure 13. Calculated natural frequencies versus rotational speed
- Figure 14. Calculated deformed mode shapes for modes 1 and 2
- Figure 15. Calculated deformed mode shapes for modes 3 and 4
- Figure 16. Airfoil mode shape cross-sections at strip no. 1
- Figure 17. Turbine blade fluid velocity diagram at strip no. 1

- Figure 18. Steady flow Mach number contours for strip no. 1
- Figure 19. Steady flow Mach number contours for strip no. 3
- Figure 20. Turbine blade surface Mach number distributions
- Figure 21. Turbine blade surface static pressure distributions
- Figure 22. Turbine blade unsteady surface pressure distributions (real part) due to motion in second mode (edgewise)
- Figure 23. Turbine blade unsteady surface pressure distributions (imaginary part) due to motion in second mode (edgewise)
- Figure 24. Turbine blade unsteady aerodynamic work per cycle distribution due to motion in second mode (edgewise)
- Figure 25. HPOTP turbine rotor tuned root locus for vibration in first mode (bending)
- Figure 26. HPOTP turbine rotor tuned root locus for vibration in third mode (edgewise), mechanical damping neglected
- Figure 27. HPOTP turbine rotor tuned root locus for vibration in second mode (edgewise), mechanical damping neglected
- Figure 28. HPOTP turbine rotor tuned root locus for vibration in second mode (edgewise), 1 % mechanical damping included

## LIST OF TABLES

- Table I.      HPOTP turbine aeroelastic strip properties
- Table II.     HPOTP turbine calculated natural frequencies

## NOMENCLATURE

### Symbols

$a$  = Fluid sonic velocity

$[A]$  = Modal unsteady aerodynamic matrix, eq (23)

$b$  = Airfoil semichord length

$B_x$  =  $c \cos \xi$  Airfoil projected chord length at stagger angle

$c$  =  $2b$  Airfoil chord length

$\bar{C}_p$  =  $\frac{\bar{p} - \bar{p}_\infty}{\frac{1}{2} \rho V^2}$  Static pressure coefficient

$\tilde{C}_p$  =  $\frac{\tilde{P}}{\rho V^2}$  Harmonic unsteady pressure coefficient

$[C]$  = Mechanical and structural damping matrix

$[C_G]$  = Generalized damping matrix, eq (14)

$\{F_A(t)\}$  = External aerodynamic forcing function

$\{F_M(t)\}$  = External mechanical forcing function

$h$  = fluid specific enthalpy

$i$  =  $\sqrt{-1}$

$k$  =  $\frac{\omega b}{V}$  Reduced frequency

$[K]$  = Structural stiffness matrix

$[K_G]$  = Generalized stiffness matrix, eq (14)

$[K^*]$  = State-space modified stiffness matrix, eq (27)

$M$  = Mach number

$[M]$  = Structural mass matrix

$[M_G]$  = Generalized mass matrix, eq (14)

- $[M^*]$  = State-space modified mass matrix, eq (27)
- $n$  = Number of degrees-of-freedom in physical space
- $\vec{n}$  = Airfoil surface normal vector
- $N$  = Number of rotor blades
- $P$  = Fluid pressure
- $\bar{P}$  = Steady-state fluid pressure
- $\tilde{P}$  = Harmonic unsteady fluid pressure
- $\{q\}$  = Vector of time dependent modal coordinates
- $\{\bar{q}\}$  = Vector of harmonic modal coordinates, eq (19)
- $\{Q\}$  = Vector of generalized forces, eq (15)
- $\{Q_A\}$  = Vector of aerodynamic generalized forces, eq (16)

$\{Q_M\}$  = Vector of mechanical generalized forces, eq (16)

$\vec{r}$  = Airfoil displacement vector

$\{R\}$  = Vector of modal unsteady aerodynamic forces

$[R]$  = Modal unsteady aerodynamic force matrix

$t$  = time

$\{u\}$  = Vector of physical displacements

$\vec{V}$  = Fluid velocity vector

$V_t$  = Fluid velocity vector tangent to airfoil surface

## Greek

$\alpha$  = Absolute flow angle

$\beta$  = Relative flow angle

$\gamma$  = Gas specific heat ratio

$\zeta$  = Modal damping ratio

$\lambda$  = Complex aeroelastic eigenvalue, eq (30)

$\mu$  = Real part of complex eigenvalue  $\lambda$ , eq (30)

$\nu$  = Imaginary part of complex eigenvalue  $\lambda$ , eq (30)

$\xi$  = Cascade stagger angle measured from axial direction

$\{\mathcal{E}\}$  = Vector of time-dependent state-space modal coordinates, eq (25)

$\{\bar{\mathcal{E}}\}$  = Vector of harmonic state-space modal coordinates, eq (25)

- $\rho$  = Fluid density
- $\sigma$  = Interblade phase angle
- $\vec{\tau}$  = Airfoil surface tangent vector
- $\phi$  = Scalar velocity potential
- $\tilde{\phi}$  = Harmonic unsteady velocity potential
- $\Phi$  = Steady-state velocity potential
- $\{\phi_n\}$  = Free-vibration natural mode shape vector
- $[\Phi]$  = Free-vibration modal matrix
- $\omega$  = Radian frequency
- $\omega_f$  = Assumed flutter frequency
- $\omega_n$  = Free-vibration natural frequency



## CHAPTER 1 - INTRODUCTION

### 1.1 Introduction

The development of propulsion system technology during the last forty years has encountered and overcome many technological barriers. Several problems associated with advanced high temperature materials, turbine cooling, and fuels and combustion were resolved with the end result of significantly higher component efficiencies and reduced fuel consumption. For gas turbine powerplants, these advances led to lighter overall designs and higher power densities compared to earlier designs. The accomplishments of lighter designs for the turbomachinery components also led to some drawbacks due to the reduced margins on the design factor-of-safety.

Fan and compressor designs during this period placed primary emphasis on higher aerodynamic loadings, and lighter blade weight to increase the gross power without sacrificing fuel efficiency. This trend led to increasingly frequent problems resulting from aerodynamic and structural interactions. A particularly serious problem was due to aeroelastic instability, flutter, which began to occur more often. This was a surprising problem because the technical consensus at the time considered that

turbomachinery blading had sufficiently high stiffness and strength to avoid aeroelastic problems.

Aeroelasticity is a science concerned with the mutual interactions among the structural (inertial and elastic) and aerodynamic characteristics of a structure immersed in a flowing fluid. Under certain conditions, when a vibrating structure begins to extract energy from the flowing fluid the structure will experience self-excited vibration. This self-excited vibration is a dynamically unstable condition, and is referred to as flutter. Up to 1960, the most common use of aeroelasticity theory was focused on the analysis of aircraft structures. Static aeroelasticity associated with wing divergence and dynamic aeroelasticity and flutter control were areas of active research for structures subjected to external flow, such as aircraft structures.

The aeroelastic problems which began to occur for systems under internal flow, i.e. turbomachinery, resulted from a combination of (a) lighter and higher stressed blade designs operating at (b) higher fluid velocities relative to fixed wing external aircraft structures. Successful solution of the aeroelastic problems in turbomachinery required more robust mechanical designs like the incorporation of part-span and tip shrouds and the use of lacing wires and intentionally introduced friction damping. Unfortu-

nately, these mechanical modifications resulted in an increase in component weight in addition to a degradation in the aerodynamic performance of the machine.

Designers of modern propulsion systems have discovered that multidisciplinary effects must be considered in order to achieve reliable turbomachinery designs. The interaction of the distinct physical processes of fluid dynamics, structural dynamics and thermodynamics of the entire engine system is becoming more important. The traditional method of designing for aerodynamic performance, independently of the structural dynamics of the system is no longer a viable approach.

The application of aeroelasticity theory to propulsion systems has enjoyed considerable attention during the time period from 1960 to the present. Advances in methods for computational fluid dynamics (CFD) and finite element analysis methods have greatly expanded the applications of aeroelastic theory. Current methods for predicting aeroelastic stability (flutter) rely upon a variety of unsteady aerodynamic models, from simple flat-plate representations of the blade up to complicated CFD analyses.

## 1.2 Literature Review

A thorough review of turbomachinery aeroelasticity requires an understanding of the physical mechanisms which dominate this type of problem. There are basically two physical processes which interact with one another within an aeroelastic system. These processes are (a) the unsteady aerodynamic behavior and (b) the structural dynamic behavior of the turbomachinery blading. The unsteady aerodynamic problem is concerned with estimating the aerodynamic response of a blade which is undergoing a periodic oscillation. This problem is complicated due to the fact that there is a transfer of energy between the blade and the flowing fluid. The structural dynamics of turbomachinery blading requires the study of the dynamic response of the blade under both free and forced vibration conditions. Aeroelasticity is an investigation of these combined aerodynamic and structural dynamic effects.

The review of previous work within the field of turbomachinery aeroelasticity is presented in the following order. A survey of the occurrence of aeroelastic problems, most notably self-excited vibrations or flutter, for various types of turbomachinery including aircraft engine fans, compressors and turbines is presented. This is followed by an examination of some of the fluid dynamic models which have been proposed to

solve the unsteady aerodynamic problem of oscillating airfoils under several different flow regimes. Finally, a review of aeroelastic models which have been applied to turbomachinery analyses over the past thirty years is included.

### 1.21 Turbomachinery Aeroelastic Problems

Reports of aeroelastic instability, or flutter, occurring in actual turbomachinery such as aircraft engines or power generation turbines are relatively rare. This is not unexpected, because the design and development of high-energy gas turbines represents a very expensive undertaking, often requiring millions of dollars and many years of design work prior to customer acceptance or certification. Some instabilities are reported in the literature, either as a result of catastrophic failures, or development delays in highly visible aerospace projects. Gas turbine manufacturers are often quick to publish results when such problems come into common knowledge in order to prove that a redesign will perform successfully.

Carter and Kilpatrick [1] were one of the first to publish an investigation of the aeroelastic response of a multi-stage compressor operating under part-speed conditions. Their experiments were conducted on the

compressors of power generation turbines to determine the vibratory stresses on the stator vanes during stall flutter and rotating stall conditions. The results from their experiments led to the introduction of some modified design correlations based on reduced frequency and incidence angle limits for high-speed compressors.

Jeffers and Meece [2] present a diagnosis of a fan stall flutter occurrence for the Pratt & Whitney F100 turbofan engine which was discovered during engine development testing. Stall flutter was found to occur for the first-stage fan at high Mach numbers under off-design conditions near the surge threshold of the engine. The fan was designed using the standard empirical correlation rules employed for all of Pratt & Whitney's engine designs up until that year. A full structural redesign of the fan including airfoil thickening and the modification of the part-span shroud was required to overcome the flutter problem. The authors expressed the need for a more reliable subsonic flutter prediction system to augment the existing empirical database which at that time was the standard technique used for aeroelastic design.

An outline of the aeroelastic design system used by General Electric was described in the work of Cardinale, Bankhead and McKay [3]. This paper presents a general overview of the empirical design system which had

been verified over several years of engine testing and in-service operation of aircraft gas turbine engines. A detailed discussion of turbomachinery mechanical and aerodynamic design, including the experimental identification of aeroelastic problems is also included. A strong conclusion from this paper is that the inherent complexities of turbomachinery, due to variations in operating conditions and flight envelopes, require the application of conservative design rules based on thousands of hours of existing engine test experience.

Aeroelastic problems are not solely limited to aircraft gas turbine engines. However, these engines are more prone to these problems because of the stringent thrust/weight requirements of propulsion systems relative to other types of gas turbines. A flutter problem encountered within the last stage turbine of a Westinghouse industrial combustion turbine was documented by Scalzo, Allen, and Antos [4]. The problem was found to occur within the last stage turbine under operating conditions where the inlet air density was high relative to normal operation. High-cycle fatigue cracking was caused by a self-excited vibration in the first bending mode of the blade. A rotor-based telemetry system was used to quantify the vibratory stress levels under hostile high temperature operating conditions [5]. The turbine blade was redesigned to stiffen the base of the blade and to increase the natural frequency of the blade, thus giving more

acceptable margin for flutter. Large amplitude dynamic response due to buffeting was also reported for the blades which did not flutter, although the large response is probably attributable to extremely low aerodynamic damping for those blades.

The impact of higher energy costs during the 1970's led to the development of high-efficiency aircraft propulsion systems, most notably the advanced turboprop or propfan engine. This engine concept replaced the standard fan of the modern turbofan with a high bypass ratio propeller-like fan, hence the name propfan. The NASA Lewis Research Center (LeRC) development and testing of propfan concepts during the early 1980's. An unexpected flutter instability occurred for the propfan denoted SR-5 and it is reported in Mehmed, Kaza, Lubomski and Kielb [6]. This propfan was made up of highly swept and twisted flexible blades which experienced classical subsonic coupled bending-torsion flutter. Different numbers of blades were tested on the rotor and the effect of the increased aerodynamic coupling due to higher blade numbers led to a stronger destabilization of the rotor.

The occurrence of classical flutter in the SR-5 propfan led to an effort to develop more accurate aeroelastic analysis for propfan design. A propfan test model was designed by NASA LeRC intentionally to encounter flutter

in the wind tunnel. This propfan designated SR3C-X2 (Mehmed and Kaza [7]) was a composite blade designed using a specific ply layup to result in natural frequencies and mode shapes which would lead to flutter of the blade under test conditions. Their work verified the accuracy of the aeroelastic analysis methods by demonstrating that a blade could be designed which would flutter at a specific operating condition.

### 1.22 Unsteady Aerodynamic Models

The underlying physics of an aeroelastic problem requires that the fluid pressure response due to the blade vibration be determined. The development of unsteady aerodynamic models for the motion-dependent behavior of cascades can be classified in a variety of ways. The most common distinction is made for blades where the influence of airfoil shapes can or cannot be neglected. A further complication to the analysis is that the unsteady aerodynamic behavior is governed by separate equations depending upon if the flow is subsonic, mixed subsonic/supersonic (transonic), or fully supersonic. The following discussion of unsteady aerodynamic models attempts to cover some of the efforts within each of the flow regimes which modern turbomachinery operates in.

One of the first investigations of the inviscid, incompressible unsteady aerodynamics of cascades of blades was reported by Whitehead [8,9]. His technique was to solve for the unsteady vorticity distribution along flat plates which were undergoing rigid translational and rotational harmonic oscillations. The airfoil vibration was applied as a boundary condition by modifying the velocity upwash along the airfoil surface. The first paper [8] was limited to flows over flat plates which caused no steady flow deflection, a truly unloaded flat plate representation of the blades. His later work [9] extended the analysis to account for the steady aerodynamic loading in the boundary condition gradient terms. The agreement of the unsteady aerodynamic results was much better with experimental data when the steady loading was included in the unsteady analysis.

This finding implied that the effect of steady aerodynamic loading was important for the unsteady aerodynamics of airfoils, even when modeled using simplified, flat plates in incompressible flows. Atassi and Akai [10] developed an approach for incompressible flows over airfoils having thickness and camber operating within a nonuniform steady flowfield. They discovered that airfoil shape and steady aerodynamic loading had a very strong influence over the unsteady aerodynamic response of oscillating cascades.

Requirements to reduce the noise problem associated with aircraft engine fans and compressors presented the need to address compressible flows, and the acoustic properties of turbomachinery operating within such flows. A development for the unsteady subsonic flow within cascades of oscillating flat plates has been reported by Smith [11]. This work was primarily concerned with quantifying the acoustical properties of the cascade by placing special emphasis on the identification of "acoustic resonance" phenomena for the cascade. The occurrence of acoustic waves greatly complicated the compressible unsteady flow problem when compared to the incompressible flows.

Namba [12] advanced a similar technique for application to subsonic cascades of flat plates operating under steady aerodynamic loading due to flow incidence. This work concluded that as for the incompressible case, the effect of steady aerodynamic loading had a considerable influence over the unsteady blade forces. Ni [13] presented a complete unsteady aerodynamic analysis for unloaded flat plates for application to both subsonic and supersonic flows. A thorough discussion of the identification of the acoustical characteristics of oscillating airfoils within these flow regimes was presented.

The development of higher tip speed fans and compressors during the 1970's opened up a unique flow regime for unsteady aerodynamic research. Operation of turbomachinery at supersonic blade tip rotational speeds and subsonic flight speeds results in a special flow problem termed "supersonic flow with subsonic leading-edge". This flow condition develops when leading edge Mach waves form but do not pass into the cascade because the axial flow velocity remains subsonic. A trailing edge Mach wave also forms and it impinges upon the adjacent blades in the cascade. Considerable effort was devoted to this supersonic flow problem because supersonic torsional flutter was becoming more frequent in the new high-speed designs.

Verdon [14] developed a velocity potential method for solving the supersonic flow with subsonic leading-edge problem for a cascade consisting of a finite number of oscillating airfoils. The method incorporated an analytical solution for the potential upstream of the cascade leading edge line matched to a finite-difference solution within the cascade region and the wake region of the cascade. The Laplace transform solution of Kurosaka [15] allowed analysis for infinite cascades of blades, which presented considerable improvement in computational time over Verdon's approach. This formulation resulted in closed-form analytical solutions

for the blade unsteady forces which could be solved quickly on the computer, although the technique was limited to low reduced frequencies.

Verdon and McCune [16] presented an approach based on a Laplace transform solution which had application to the full range of reduced frequencies. A similar solution using the Wiener-Hopf technique was described in the work of Adamczyk and Goldstein [17]. This method results in a full analytical solution for the unsteady flow problem. Adamczyk and Goldstein's model is popular and widely used in the turbomachinery field.

Miles [18] initiated the unsteady aerodynamic work for flows which had supersonic axial flow over the leading edge of the blade in 1956. Lane [19] presented a similar analysis which evaluated the integral equations and accounted for the Mach wave reflections in the blade-row. Interest in supersonic transport in the late 1980's led to renewed interest in the analysis of supersonic axial flow. Ramsey and Kielb [20] developed an algorithm for solving the formulations of Miles and Lane efficiently on a computer.

Most of the methods discussed to this point have considered the cascade to consist of flat plates, or cascades where the steady flow was fully uncoupled from the unsteady flow. Ni and Sisto [21] presented an approach

which solved the unsteady Euler equations for a cascade of blades using a time-marching integration method. The work was limited to flat plate airfoils undergoing harmonic motions, but the method was one of the first to solve the unsteady Euler equations using a finite-difference solution. A key feature of the method was that the mean steady-state flow was fully coupled to the unsteady flow in the cascade. A disadvantage of the approach was that the time integration resulted in long computer running times.

Another time integration solution for the unsteady Euler equations was presented by Huff and Reddy [22]. They employed a deforming grid method for solving the unsteady Euler equations for cascades of supersonic fan blades modeled using a finite-difference strategy. They presented results for a flat plate cascade and compared the solution using the unsteady Euler equations and a small-disturbance supersonic theory which showed excellent agreement. Results were also included for a highly cambered supersonic fan blade undergoing torsional oscillation. Disadvantages of this method were excessively long computer running times and a limitation which required multiple computational grids for small interblade phase angles.

Verdon and Caspar [23] developed a solution method for the unsteady potential equation by linearizing the unsteady flow about a nonuniform steady flowfield. The thickness and camber of the airfoils in the cascade was accommodated by solving the unsteady potential as being a small disturbance about the nonuniform steady potential field. The nonlinear steady full potential flow was coupled to the harmonic unsteady potential caused by blade vibration. Results showed the effect of airfoil shape and flow incidence with comparison to flat plate analysis. An advantage of this method was that a direct matrix solution for the unsteady potential was obtained compared to iterative solutions commonly used in CFD applications. The direct solution scheme results in reduced computational time.

The transonic unsteady flow problem was investigated by Verdon and Caspar [24] in 1984. The linearized unsteady potential flow theory was used to model flows containing weak cascade shocks. The shocks were assumed to undergo small-amplitude harmonic motion during airfoil oscillation. The unsteady flow was assumed to be a first-order harmonic perturbation of the nonlinear steady flow field. Shock fitting was used to model the unsteady shock motion. Whitehead [25] presented a solution for the linearized unsteady potential equation which was similar to the method of Verdon although his approach utilized a finite element solution scheme. This technique also used a shock-capturing method for the

steady flow, although the results compare very well with those of Reference [24].

### 1.23 Aeroelastic Analysis Models

System energy models were commonly used to predict flutter inception in turbomachinery prior to 1970. The unsteady aerodynamic loads were modeled using isolated airfoil thin-wing theories which were developed for aircraft aeroelastic analysis. These isolated airfoil theories were often applied at the 3/4 span location of the blade, and an assessment of the work that the aerodynamic loads performed could be determined by considering the unsteady aerodynamic forces and the blade mode shape. Stability was determined based on whether the work of the fluid on the blade was either positive (unstable) or negative (stable). An example of this type of model is described by Carta [26]. His work was principally concerned with studying the effect of blade-disk-shroud structural dynamic coupling, although the isolated airfoil theory was incorporated to simulate blade-to-blade aerodynamic coupling.

A need for higher pressure ratios and increased thrust in the 1970's resulted in turbomachinery having higher tip speeds. Aeroelastic modeling utilizing the new unsteady aerodynamic models for turbomachinery more

accurately estimated the onset of flutter. Snyder and Commerford [27] used an energy method which applied the supersonic/subsonic leading edge model of Verdon [14] to predict flutter of high-speed fan flutter. In addition, they also performed an experiment in a linear cascade of seven oscillating blades to measure when flutter would occur for ranges in Mach number and frequency. The agreement between the supersonic unsteady aerodynamic model and the measured flutter conditions was very good. It was noted that the cascade effects of the adjacent blades caused the system to be less stable than the isolated airfoil theory predicted, and they concluded that cascade unsteady aerodynamic theory must be used for the unique unsteady flows of turbomachinery.

A description of the flutter prediction model used by Pratt & Whitney Aircraft in 1975 is outlined in the work of Mikolajczak, et. al. [28]. This work discovered that the empirical correlations and design rules formerly used were inadequate for flutter analysis of high-speed flows. The aeroelastic model was an energy model where the sum of the calculated aerodynamic and structural damping was used as a measure of stability. The model incorporated unsteady aerodynamic theories of Whitehead [8], Smith [11], and Verdon [14] for estimation of unsteady aerodynamic forces in the incompressible, subsonic, and supersonic flow regimes. This work em-

phasized the importance of accurate blade vibrational analysis, blade-disk structural coupling, and unsteady aerodynamic forces in flutter analysis.

The aeroelastic models up to 1980 were primarily based on energy methods, where the blades were assumed to vibrate in a single degree-of-freedom or in a single vibrational mode. A new trend in flutter analysis was to include multiple degrees-of-freedom for the blade and to investigate the effect of coupling on blade flutter. Bendiksen and Friedmann [29] presented an aeroelastic model which incorporated two degrees-of-freedom (DOF) for the blade. This approach utilized the incompressible cascade theory of Whitehead [8]. A lumped parameter model of a "typical section" along the span of the blade was used which had one bending and one torsional degree-of-freedom. The results imply that bending-torsion coupling can have a pronounced effect on cascade flutter, and that accurate aeroelastic analysis must account for multiple degrees-of-freedom.

The lumped parameter two DOF model became the most commonly used approach for aeroelastic analyses during the 1980's, and serves as the workhorse of modern turbomachinery flutter analysis. The combination of the unsteady aerodynamic theories of Smith [11], Adamczyk and Goldstein [17], and Ramsey and Kielb [20] combined with the coupled bending-torsion two DOF blade description has resulted in flutter predic-

tion models which are relevant for all of the flow regimes of modern turbomachinery.

All of the aeroelastic models discussed assume that each blade within a rotor is identical, having exactly the same natural frequencies and mode shapes. This system is termed a "tuned" system. Research to determine the aeroelastic behavior of systems which have small statistical variations in dynamic properties of the adjacent blades on the rotor has begun. Such a rotor is referred to as "mistuned" because the dynamic behavior of the rotor is no longer uniform from blade-to-blade. A study of mistuned systems ([30] to [33]) has concluded that the tuned system represents the most unstable configuration for a rotor. Mistuning has a stabilizing effect on the flutter stability of rotors, primarily due to a break-up of the cyclicity of the rotor. This was an important conclusion because the analysis of mistuned rotors was computationally expensive, and knowledge that the tuned analysis is conservative simplifies the turbomachinery designer's task.

The occurrence of flutter in the SR-5 advanced propfan indicated that a flutter problem existed which could not be predicted using the available aeroelastic analysis methods. The propfan was a thin, swept, flexible propeller blade which experienced large-amplitude self-excited vibration

during performance testing at NASA LeRC [6]. The complicated vibrational behavior of the blade could not be properly predicted using a simple typical section two DOF aeroelastic model.

Nonlinear large-displacement beam structural dynamic models were introduced in order to incorporate the three-dimensional properties of the blade. Kaza and Kielb [34], [35] developed an analysis which modeled the blades as cantilevered beams having varying properties along the span. The model also accounted for the effects of centrifugal stiffening of the beam. The unsteady aerodynamic forces were evaluated at several radial positions along the span of the beam and the forces were numerically integrated along the span to arrive at an unsteady aerodynamic generalized force. The unsteady aerodynamic models used were those of Smith [11] for subsonic flows and Adamczyk and Goldstein [17] for supersonic flows.

The beam models of the propfans resulted in better analytical prediction of the experimental flutter conditions. But the wind tunnel propfan models underwent complicated coupled vibrational modes, which could not be fully simulated using the beam representation. The finite element method was chosen to model the propfan blades so that the simulation of the flexible blade dynamics could be accomplished more accurately.

Turnberg [36] first applied the finite element method to the analysis of propfan flutter in 1983. He used modal analysis to base the aeroelastic response on the in-vacuum free vibration modes of the blade. The subsonic theory of Smith [11] was used to determine the unsteady aerodynamic forces acting at several "strips" along the span of the blade. The comparison with experimental results was very good. A disadvantage of the method was that the aerodynamic model assumed that the flow on each strip was two-dimensional, even though experimental flow visualization found that large spanwise flows occurred for the propfan blades.

An extension of the finite element based modal aeroelastic analysis was developed by Kaza, et. al. [37] by incorporating a three-dimensional unsteady aerodynamic theory. The aerodynamic model used a lifting surface theory to model the blade using oscillating doublets which were placed on panels along the three-dimensional surface of the blade. This approach showed excellent agreement with the wind tunnel experiments for flutter prediction over a wide range of speeds. The primary limitation of the lifting surface aerodynamic model was that the airfoil was modeled as a zero-thickness camber line with zero flow incidence.

### 1.3 Objective of Current Work

The purpose of this work is to present the development and application of an aeroelastic stability analysis which is suitable for all types of axial-flow turbomachinery. A review of the related previous work has discovered most of the aeroelastic analyses developed to date have been restricted to two degree-of-freedom lumped parameter models or flat plate small-disturbance unsteady aerodynamic models which disregard the effects of steady aerodynamic loading. The unsteady aerodynamic models which account for steady aerodynamic loading often require considerable computer running times which prevent their use within production aeroelastic codes. Based on the results of the literature review, the present work was begun with the objectives to:

- Develop an aeroelastic stability analysis suitable for general axial-flow turbomachinery blade designs having varying degrees of airfoil camber and thickness and operating in compressible flows.
- Utilize two-dimensional steady full potential and linearized unsteady potential flow theory to calculate the motion-dependent aerodynamic loads acting on the blade during vibration.

- Account for three-dimensional aeroelastic effects by calculating the unsteady aerodynamic loads on two-dimensional strips which are stacked along the span of the blade from airfoil hub to tip.
- Use modal analysis to couple the in-vacuum natural vibrational modes of the blade to the motion-dependent unsteady aerodynamic loads within the frequency domain.
- Demonstrate capability by applying method to a high-energy subsonic turbine rotor blade which is suspected to experience aeroelastic problems.

The implementation of this analytical formulation was performed at NASA LeRC in support of their turbomachinery aeroelasticity research. NASA LeRC is developing an aeroelastic analysis for turbomachinery called the Forced REsponse Prediction System (FREPS) which is applicable to flutter and forced response prediction for fans, compressors, and turbine blades.

## CHAPTER 2 - ANALYTICAL DEVELOPMENT

### 2.1 Aerodynamic Analysis

The fluid flow within the turbomachinery blading is modeled along stacked two-dimensional streamsurface "strips" over the blade from the airfoil hub to tip. This model is a simplification of the three-dimensional flows which occur in turbomachinery blades. However, it is fair to assume that the streamsurfaces for a high hub/tip ratio turbomachine are almost two-dimensional, except close to the hub and the tip of the blade where secondary flows dominate.

The linearized potential theory of Verdon and Caspar [24] is used to model the unsteady flow within the blades. This linearized potential approach assumes that the unsteady flow resulting from airfoil oscillation is a small perturbation of the nonlinear steady-state (or "mean") flow. It is assumed that the primary influence of blade thickness and camber on the unsteady flow is due to the motion of the airfoil through the nonuniform steady flowfield. The steady full potential flowfield is evaluated prior to solution of the unsteady potential flow in order to account for the coupling of the steady and unsteady flows. A brief description of the governing equations and solution for both the steady full potential flow and the

linearized unsteady potential flow follows. A detailed review of the steady and unsteady aerodynamic formulation used may be found in Verdon [38].

### 2.11 Steady Full Potential Flow

The steady compressible flow along a two-dimensional surface is calculated using the full potential method of Caspar, et. al. [39]. A finite-area technique is utilized to solve the continuity equation for a single blade passage. For compressible, inviscid, isentropic, and irrotational steady flow of a perfect gas, the continuity equation can be solved uniquely for the steady flow.

$$\nabla \cdot (\rho \vec{V}) = 0 \quad (1)$$

In terms of the velocity potential, equation 1 yields the steady full potential equation (equation 2).

$$\nabla \cdot (\rho \nabla \Phi) = 0 \quad (2)$$

The flow variables  $\rho$  and  $\vec{V}$  are nondimensionalized by their values at the inlet of the passage denoted as state 1. This nondimensionalized

equation, along with the steady Bernoulli equation and the ideal gas equation of state results in an expression for the local density.

$$\rho = \left[ 1 - \frac{(\gamma - 1)}{2} M_1^2 (\nabla\Phi \cdot \nabla\Phi - 1) \right]^{\frac{1}{\gamma - 1}} \quad (3)$$

The inlet Mach number at state 1 is  $M_1$  and the specific heat ratio of the gas is  $\gamma$ . The steady potential flow within the cascade may be solved using the continuity equation of eq (2) and the local density description of eq (3). The solution is also solved for weak shock waves for which the flow is assumed to remain isentropic and irrotational. The steady flow analysis incorporates an artificial viscosity scheme in supersonic regions to stabilize the calculations (by Caspar [40]).

Figure 1 includes a figure showing a two-dimensional representation of the cascade with the inlet and exit flow velocity vectors indicated. A diagram of the cascade geometry, including the stagger angle, airfoil chord, cascade gap and the leading and trailing edges is included on figure 2. The regions where the boundary conditions for the full potential equation are applied are shown on the blade-to-blade cascade of figure 3.

The boundary conditions for the mean potential flow require the airfoil surface flow tangency condition (equation 4).

$$\nabla\Phi\cdot\vec{n} = 0 \quad \text{along the airfoil surface} \quad (4)$$

An additional boundary condition is applied at the periodic boundaries as

$$\nabla\Phi_{lower\ periodic} = \nabla\Phi_{upper\ periodic} \quad (5)$$

which states that the flow is continuous across the periodic boundaries. The boundary condition at the upstream boundary 1 requires specification of the inlet Mach number  $M_1$  and the inlet flow angle  $\beta_1$ .

The airfoil is assumed to have a sharp trailing edge, such that the Kutta condition may be satisfied. The addition of a wedged trailing edge also simulates the viscous interaction of the upper and lower surface flows which meet at a blunt trailing edge. This Kutta condition allows the downstream flow angle  $\beta_2$  to be prescribed as the bisector of the blade trailing edge metal angle. The overall mass conservation can then be solved for the downstream exit Mach number  $M_2$ .

The finite-area solution of equation (2) requires the use of a spatial mesh to discretize the flow passage. The approach of Reference [40] uses two spatial meshes for the mean flow solution. An H-type of computational mesh is used to capture the overall flow details of the passage. A C-type

of computational mesh is also used to resolve the finer flow details around the leading edge (LE) stagnation point and around shocks. Examples of these types of meshes are shown on figure 4. The mass conservation equation is applied to the cells of the finite-area mesh for the solution of equation (2). A successive line over-relaxation scheme is used to iteratively solve the nonlinear steady potential equation.

### 2.12 Linearized Unsteady Potential Flow

The unsteady flow, i.e. that flow caused by airfoil oscillation, is calculated using the linearized potential approach of Verdon and Caspar [24]. The unsteady flow is modeled as a small-amplitude potential perturbation from the steady potential flow. The unsteady potential is a scalar representation of the velocity which requires that the unsteady flow remain irrotational and isentropic. The airfoils in the cascade are assumed to vibrate with small-amplitude harmonic motion and a constant phase angle between adjacent blades.

These assumptions permit the unsteady equations of motion for the flow to be reduced to a single partial differential equation which is solved for the harmonic unsteady potential. The unsteady potential equation is shown in nonconservative form in equation 6.

$$\frac{D^2 \tilde{\phi}}{Dt^2} + \frac{1}{2} \nabla \tilde{\phi} \cdot \nabla (\nabla \Phi)^2 + \nabla \tilde{\phi} \cdot \nabla (\nabla \Phi \cdot \nabla \tilde{\phi}) = a^2 \nabla^2 \tilde{\phi} \quad (6)$$

In this equation  $\Phi$  is the steady velocity potential and  $\tilde{\phi}$  is the unsteady velocity potential. The unsteady substantial derivative operator is  $\frac{D()}{Dt} = i\omega() + \nabla \Phi \cdot ()$ . Derivation of equation (6) from the unsteady Euler equations is shown in Appendix A.

The boundary conditions for the unsteady potential problem require specification of conditions along the upstream and downstream, vibrating airfoil surfaces, and the cascade periodic boundaries (figure 5). The surface flow tangency condition requires that the unsteady flow remain bounded by the moving airfoil surfaces. The airfoil surface may undergo any general deformation mode, as indicated in figure 6. The surface boundary condition along the airfoil is

$$\nabla \tilde{\phi} \cdot \vec{n} = \left[ \frac{\partial \vec{r}}{\partial t} + v_\tau \frac{\partial \vec{r}}{\partial \tau} - (\vec{r} \cdot \nabla) \nabla \Phi \right] \cdot \vec{n} \quad (7)$$

where  $\vec{n}$  is a unit vector normal to the airfoil surface,  $\vec{r}$  is the airfoil displacement vector,  $V_t$  is the velocity tangent to the airfoil surface, and  $\vec{\tau}$  is the unit vector tangent to the airfoil surface.

The first term of equation (7) defines the velocity of the airfoil normal to its surface during oscillation. The second term represents the rotation of the airfoil through the steady potential field. The last term extrapolates the surface boundary conditions along the surface of the oscillating airfoil to the mean location of the airfoil in the steady reference frame.

Expressing the surface boundary conditions of the oscillating airfoil at the steady airfoil location permits solution on a stationary, nondeforming computational grid. A Taylor series expansion of the moving airfoil location relative to the steady airfoil location is applied to extrapolate the boundary conditions to the steady airfoil surfaces. First-order (linear) terms are retained in this series expansion (Reference [38]) which results in the last term of equation (7).

Substitution of the harmonic time dependence into equation (7) results in the surface boundary condition of equation (8).

$$\nabla\tilde{\phi}\cdot\vec{n} = [i\omega\vec{r} + (\nabla\Phi\cdot\vec{\tau})(\vec{\tau}\cdot\nabla)\vec{r} - (\vec{r}\cdot\nabla)\nabla\Phi]\cdot\vec{n} \quad (8)$$

The periodic boundary condition for the unsteady potential is prescribed as a constant phase angle difference in time for the adjacent blade in the cascade. Since the airfoil is assumed to undergo harmonic motion, the solution for flow passages adjacent to the computational passage simply vary by a constant harmonic "interblade phase angle"  $\sigma$  (see figure 5). The adjacent blade's harmonic motion in terms of the interblade phase angle is given by equation (9).

$$\vec{r}_{j+1} e^{i\omega t} = \vec{r}_j e^{i(\omega t + \sigma)} \quad (9)$$

The  $j$  represents the blade number on the rotor. All of the flow variables are assumed to vary between adjacent flow passages by this interblade phase angle relationship. The upstream and downstream boundary conditions are determined from analytical expressions for the far-field potential fluctuations due to blade oscillation.

The equation for the unsteady potential is solved using a weighted least-squares finite difference discretization. Differencing weights are determined from the coefficient terms of equation (6). The blade passage is discretized using the same type of global and local computational meshes as described for the steady potential computation (figure 4). Solution for

the unsteady potential is obtained by a direct matrix solution of equation (6).

The unsteady pressure  $\tilde{P}$  is found from the unsteady expansion

$$\tilde{P} = \tilde{p} + (\vec{r} \cdot \nabla) \bar{P} \quad (10)$$

where  $\tilde{p}$  represents the harmonic pressure and the second term represents the first-order Taylor series expansion for the pressure variation due to the airfoil motion through the steady potential and pressure fields.

The harmonic pressure is calculated from the unsteady potential as

$$\tilde{p} = -\bar{\rho} \frac{D\tilde{\phi}}{Dt}$$
$$\tilde{p} = -\bar{\rho}(i\omega\tilde{\phi} + \nabla\Phi \cdot \tilde{\phi}) \quad (11)$$

The unsteady forces and moments acting on the airfoil are determined by integrating the harmonic pressure of equation (10) over the airfoil surface.

The unsteady flow problem described in this section is determined for a prescribed set of steady flow and unsteady flow parameters. The steady flow parameters for a particular airfoil geometry and working fluid are (a)

the inlet Mach number  $M_1$  and (b) the inlet flow angle  $\beta_1$ , where the exit Mach number and angle are determined from the trailing edge Kutta condition. The unsteady flow parameters are (a) the blade displacement vector  $\vec{r}$ , (b) the interblade phase angle  $\sigma$ , and (c) the vibrational reduced frequency  $k = \frac{\omega b}{V}$ .

The nondimensional reduced frequency  $k$  is a measure of the unsteadiness of the flow. In general, the reduced frequency can be viewed as the ratio of the time a fluid particle takes to pass over the surface of the blade, i.e. proportional to  $\frac{b}{V}$ , compared to the time it takes to complete one cycle of blade vibration  $\frac{1}{\omega}$ . Thus, when the reduced frequency is low, i.e. less than or equal to 0.5, the flow is varying in approximately the same fashion as the excitation. This situation can lead to large unsteady aerodynamic forces. Likewise when the reduced frequency becomes high, i.e. larger than 0.5, the excitation is much higher than the fluid particle velocity and the flow has little time to react to the excitation. Flows at higher reduced frequencies usually result in relatively low unsteady aerodynamic forces.

## 2.2 Structural Dynamic Analysis

Dynamic analysis of blades of general shape is most efficiently accomplished using the finite element method (FEM). The FEM permits a

straightforward method for estimating the dynamics of blades having complex geometries and being made of advanced anisotropic materials.

The dynamic equations of motion for the finite element representation of the blade are shown below

$$[M]\{\ddot{u}\} + [C]\{\dot{u}\} + [K]\{u\} = \{F_A(t)\} + \{F_M(t)\} \quad (12)$$

where the  $n$  global degrees-of-freedom (DOF) displacements are  $\{u\}$ . The structure mass, damping, and stiffness are represented by the matrices  $[M]$ ,  $[C]$ , and  $[K]$ , respectively. The forcing terms on the right-hand side of equation (12) represent the external forces due to aerodynamic  $\{F_A(t)\}$  and mechanical  $\{F_M(t)\}$  sources.

The undamped homogeneous form of equation (12), i.e. neglecting forcing terms and damping, represents the free vibration problem of the blade. Solution of the free vibration problem requires the solution of the real eigenvalue problem

$$\omega^2[M]\{\bar{u}\} = [K]\{\bar{u}\} \quad (13)$$

which results in the set of  $n$  eigenvalues  $\omega_n$  and eigenvectors  $\{\phi_n\}$ . These eigenvalues represent the undamped natural frequencies for the blade and the undamped natural modes, or mode shapes.

The dynamic motion of the blade, in the presence of forcing functions and damping, is assumed to be represented as a linear combination of contributions from each of a reduced set of the free-vibration natural modes. This modal expansion using  $m$  modes for the  $n$  DOF system assumes that the dynamic displacements can be written as

$$\{u(t)\} = [\Phi]\{q(t)\} \quad (14)$$

where  $[\Phi]$  is the  $n \times m$  modal matrix having the undamped eigenvectors  $\{\phi_n\}$  arranged columnwise. The vector  $\{q(t)\}$  is the time-dependent modal coordinate vector. The modal coordinates represent a measure of each of the natural vibrational mode's contribution to the dynamic displacements. The choice of which  $m$  modes to retain for the dynamic analysis depends upon the nature of the expected forcing function. The contribution of modes having high natural frequencies relative to the forcing frequency will be low. In general, only those modes having frequencies close to the expected forcing frequency or vibrating frequency need to be retained.

Substitution of equation (14) into the original dynamic equations of motion equation (12), and premultiplying by the transpose of the modal matrix

$[\Phi]^T$ , transforms the dynamic equation from physical space to modal space. The modal equation of motion becomes

$$[M_G]\{\ddot{q}\} + [C_G]\{\dot{q}\} + [K_G]\{q\} = [\Phi]^T(\{F_A(t)\} + \{F_M(t)\}) \quad (15)$$

where this equation represents  $m$  equations, so that the dynamic problem has been reduced from a system of  $n$  equations.

The following definitions are used for the transformed matrices

$$\begin{aligned} [M_G] &= [\Phi]^T [M] [\Phi] \\ [C_G] &= [\Phi]^T [C] [\Phi] \\ [K_G] &= [\Phi]^T [K] [\Phi] \end{aligned} \quad (16)$$

These matrices are known as the generalized mass, generalized damping, and generalized stiffness matrices and they are of size  $m \times m$ . The generalized mass  $[M_G]$  and generalized stiffness  $[K_G]$  matrices are diagonal due to the orthogonality of the eigenvectors to the physical mass  $[M]$  and stiffness  $[K]$  matrices.

It is difficult to accurately determine the generalized damping matrix  $[C_G]$  because of the complicated nature of damping in turbomachines. Damping for a blade is strongly dependent upon material damping, damping in connections, such as contact stresses in turbine blade roots,

and structural interfaces such as shroud gaps. These types of connections are often a nonlinear function of displacements, and a considerable amount of research has been devoted to damping models with little definite success.

A common assumption for modeling generalized damping is to assume equivalent modal damping, which is similar to single DOF damping, applied to each individual vibrational mode of the structure. The concept of modal damping results in the following diagonal generalized damping matrix

$$[C_G] = [2\zeta\omega_n] \quad (17)$$

where the modal damping ratios  $\zeta$  corresponding to each individual mode are along the diagonal.

The force expression on the right-hand side of equation (15) is referred to as the generalized force vector  $\{Q(t)\}$  and it is defined in equation (15).

$$\{Q(t)\} = [\Phi]^T (\{F_A(t)\} + \{F_M(t)\}) \quad (18)$$

Using the definitions

$$\begin{aligned}\{Q_A(t)\} &= [\Phi]^T \{F_A(t)\} \\ \{Q_M(t)\} &= [\Phi]^T \{F_M(t)\}\end{aligned}\tag{19}$$

simplifies the total generalized force as the sum of the aerodynamic generalized forces  $\{Q_A(t)\}$  and the mechanical generalized forces  $\{Q_M(t)\}$

The final form of the modal equations of motion, using the above definitions, becomes

$$[M_G]\{\ddot{q}\} + [C_G]\{\dot{q}\} + [K_G]\{q\} = \{Q(t)\}\tag{20}$$

which represents the  $m$  modal equations for the system. Note that this equation, with the assumption of modal damping, represents a system of  $m$  uncoupled, second-order ordinary differential equations. This is a significant simplification from the system of  $n$  fully coupled equations as given by equation (12). The loss of accuracy due to the modal truncation can be reduced by including more modal coordinates, and basis mode shapes, within the analysis.

### 2.3 Aeroelastic Model

The rotor for the present study is assumed to vibrate as a "tuned" rotor, where every blade on the disk has the same natural frequencies and

mode shapes. This assumption is obviously inaccurate, because every blade will have small differences due to the manufacturing process, installation effects, etc. But a tuned rotor always results in the most conservative estimate of flutter, as was discussed in section 1.23, and additionally significantly simplifies the computational effort for aeroelastic analysis.

The tuned rotor implies that the rotor blades have equal amplitudes of motions while having a constant phase lag between adjacent blades. This assumption results in a travelling wave which passes along the periphery of the rotor with a certain frequency and wavelength which corresponds to the constant interblade phase angle  $\sigma$ . A tuned rotor may vibrate with any of  $N$  possible interblade phase angles where  $N$  is the number of blades on the rotor.

The interblade phase angles are limited to the discrete values

$$\sigma_j = \frac{2\pi(j-1)}{N} \quad (21)$$

for  $j = 1$  to  $N$ . The vibration of the rotor in the  $\sigma_j$ <sup>th</sup> interblade phase angle refers to the  $j$ <sup>th</sup> travelling wave of the rotor.

Incipient flutter is a linear problem since the vibration up until it becomes unstable is small-amplitude and occurs at a definite individual frequency. Flutter prediction is concerned with identifying the conditions where the vibrations just begin to go unstable.

Since the vibrations occur at a single frequency, the modal coordinate vector can be assumed to vary harmonically in time. This is represented as

$$\{q(t)\} = \{\bar{q}\} e^{i\omega_f t} \quad (22)$$

where the vibrational frequency, i.e. the flutter frequency  $\omega_f$ , is assumed to be close to a natural frequency of the blade. Such an assumption implies that the dynamic displacements of the aeroelastic system  $\{u(t)\}$  are harmonic, and consist of a linear combination of harmonic vibrations of each undamped mode which corresponds to the modal coordinates  $\{\bar{q}\}$ .

The unsteady aerodynamic forces on the blade are applied to the blade as the external aerodynamic forces  $\{F_A(t)\}$ . When the mechanical forces are neglected, the generalized forces reduce to only the aerodynamic generalized forces (equation 23).

$$\{Q(t)\} = [\Phi]^T \{F_A(t)\} \quad (23)$$

The external aerodynamic forces may be classified as either (a) motion-dependent aerodynamic forces or (b) motion-independent aerodynamic forces. The motion-dependent forces are caused by the response of the fluid to the underlying blade motion. The pressure response of the fluid lags the motion of the blade, so that the motion-dependent forces are represented as complex having in-phase (real) and out-of-phase (imaginary) parts. The motion-independent forces result from aerodynamic excitations such as incoming pressure waves or velocity wakes, and these forces are primarily of importance in determining the forced response of aeroelastic systems. For linear flutter analysis, they play no role in the prediction of stability and will be neglected.

The motion-dependent unsteady aerodynamic forces are modeled as complex nodal loads which act at the finite element physical DOF. Since linear unsteady aerodynamic theory was assumed the full unsteady forces can be represented as a summation of the forces caused by motion at each of the natural modes of vibration of the blade. This assumption is similar to the expansion of the physical DOF using modal analysis.

Following this assumption, the motion-dependent unsteady aerodynamic forces are modeled as

$$\{F_A(t)\} = \omega_f^2 [R] \{q(t)\} \quad (24)$$

with  $[R]$  being the  $n \times m$  unsteady aerodynamic modal forces having each individual force vector  $\{R\}$  arranged columnwise, as in the modal vector  $[\Phi]$ . The force vector  $\{R\}_j$  is the unsteady aerodynamic forces acting at each blade DOF due to vibration of the blade in the  $j^{\text{th}}$  mode. The coefficient  $\omega_j^2$  results because of the scaling of the unsteady pressures by the inlet steady dynamic pressure term  $\bar{\rho}V_1^2$ .

The modal unsteady forces are strongly dependent upon the assumed flutter frequency  $\omega_j$ , interblade phase angle  $\sigma$ , inlet Mach number  $M_1$  and the rotor speed. The calculation of the modal aerodynamic forces  $\{R\}_j$  is accomplished in the following procedure:

1. Interpolate the blade mode shape  $\{\phi\}_j$  from the finite element model to the unsteady computational mesh.
2. Solve the linearized unsteady potential equation using the mode shape  $\{\phi\}_j$  as the airfoil displacement vector  $\vec{r}$ .
3. Calculate the resulting unsteady pressure  $\tilde{p}$  along the airfoil surface.
4. Integrate the surface unsteady pressure  $\tilde{p}$  along the airfoil surface to result in unsteady concentrated forces  $\{R\}_j$  which act at the finite element nodal DOF.

The resulting force vector due to the  $j^{\text{th}}$  airfoil mode shape, is the modal unsteady force vector  $\{R\}_j$ ,

Substitution of the motion-dependent force expression of equation (24) into the generalized force of equation (23) results in the following

$$\{Q(t)\} = \omega_f^2 [\Phi]^T [R] \{q(t)\}$$

or

$$\{Q(t)\} = \omega_f^2 [A] \{q(t)\} \quad (25)$$

and the modal aerodynamic matrix is

$$[A] = [\Phi]^T [R] \quad (26)$$

which is of size  $m \times m$ .

A physical interpretation of  $[A]$  is that the  $A_{ij}$  element represents the aerodynamic generalized force in the  $i^{\text{th}}$  mode caused by motion of the blade in the  $j^{\text{th}}$  vibrational mode. This matrix is in general nonsymmetric, and has complex elements which include the magnitude and phase of the generalized unsteady aerodynamic forces. The matrix also requires harmonic time variation because the unsteady aerodynamic model used is only applicable for harmonic blade motions.

Definition of the modal aerodynamic matrix permits substitution of eqs (25) and (26) into the equation of motion equation (20) to result in

$$[M_G]\{\ddot{q}\} + [C_G]\{\dot{q}\} + [K_G]\{q\} = \omega_f^2[A]\{q\}. \quad (27)$$

The harmonic motion assumption could now be applied to reduce this system to an eigenvalue problem. Unfortunately, the presence of damping in this equation prevents a straightforward eigensolution of the modal equations because they are in quadratic form. Eigenvalues of a damped system occur in complex conjugate pairs, resulting in  $2m$  eigenvalues, whereas the modal equation (27) contains only  $m$  equations.

A state vector transformation is used to express equation (27) in state space, which results in a system of  $2m$  equations for the  $2m$  eigenvalues. This transformation (Reference [41]) involves defining the auxiliary variables

$$\{\xi\} = \begin{Bmatrix} \{\dot{q}\} \\ \{q\} \end{Bmatrix} \quad (28)$$

which results in the state space representation of the system of equations

$$[M^*]\{\dot{\xi}\} = [K^*]\{\xi\} \quad (29)$$

with the modified partitioned matrices defined as

$$\begin{aligned} [M^*] &= \begin{bmatrix} [0] & ([M_G] + [A(\omega_f)]) \\ ([M_G] + [A(\omega_f)]) & [C_G] \end{bmatrix} \\ [K^*] &= \begin{bmatrix} ([M_G] + [A(\omega_f)]) & [0] \\ [0] & -[K_G] \end{bmatrix}. \end{aligned} \quad (30)$$

The state-space variables  $\{\xi\}$  are assumed to have harmonic variation in time, as

$$\{\xi\} = \{\bar{\xi}\} e^{\lambda t} \quad (31)$$

so that the transformed modal equation of equation (29) becomes the following aeroelastic eigenvalue problem

$$\lambda [M^*] \{\bar{\xi}\} = [K^*] \{\bar{\xi}\} \quad (32)$$

which is a  $2m \times 2m$  complex eigenvalue problem.

The set of complex eigenvalues from the solution of equation (32) are expressed as

$$\lambda = \mu + \nu i \quad (33)$$

where the real part ( $\mu$ ) of the eigenvalues represents a measure of the system damping, both mechanical and aerodynamic, and the imaginary part ( $\nu$ ) of the eigenvalues represents the damped natural frequency of the system.

The '2m' eigenvalues are used to assess the stability of the system for the vibration at the frequency  $\omega_f$ . The stability of the system is governed by the real part of the eigenvalues. When the real part  $\mu$  is greater than or equal to zero, the system will be unstable, with the vibration amplitude growing exponentially in time. Flutter is said to occur when  $\mu = 0$ , a neutrally stable condition, or when  $\mu > 0$ , an unconditionally unstable condition.

The eigenvalue problem represented by equation (32) requires an iterative solution because of the dependence of the modal aerodynamic matrix upon the assumed frequency  $\omega_f$ . Solution of this problem, for a specific rotor speed and Mach number, requires calculation of the modal aerodynamic matrix and damped eigenvalues for an assumed frequency  $\omega_f$ . The calculated eigenvalue of interest from equation (32) must have the frequency portion  $\nu$  equal to the assumed flutter frequency  $\omega_f$  because of

the restrictions of the unsteady aerodynamic theory. If the calculated eigenvalues are not equal to the assumed flutter frequency, the new assumed flutter frequency is set to the calculated damped natural frequency  $\omega_f = v$ . The modal aerodynamic matrix is recalculated and the eigensolution continued in this fashion until convergence is achieved.

## CHAPTER 3 - APPLICATION OF METHOD

### 3.1 Computer Program

An outline of the computer implementation of the aeroelastic model from Chapter 2 is diagrammed in figure 7. The procedure involves reading in the blade geometric information, i.e. finite element model, and also reading the free-vibration eigenvalues and eigenvectors. The free-vibration analysis is performed using either the MSC/NASTRAN or the MARC general-purpose finite element packages. The aeroelastic strip definitions are input after the blade geometry and modal information. Each strip is defined by specifying a locus of finite element nodal points along the airfoil surface. For each strip the inlet velocity triangle for the flow is specified. Additionally, the aeroelastic parameters (flutter frequency  $\omega_f$ , interblade phase angles  $\sigma$ ) are input.

Along each strip, the computational grids are generated for the calculation of the steady and unsteady potential flows. The method currently uses two different sets of grids for the steady and the unsteady flow problems. The steady flow solution for each strip is calculated and stored in database files on the computer. Similar information is initialized for the unsteady flow on each strip and stored in the database files.

FREPS begins the aeroelastic analysis by initializing the supplied database files which contain the steady potential solution and the computational grid information. The modal aerodynamic matrix is calculated using the procedure outlined in figure 8. The airfoil two-dimensional mode shapes are determined from the finite element eigenvectors for each strip. The mode shapes are interpolated from the finite element reference frame onto the unsteady aerodynamic computational grid. The unsteady flow due to the enforced airfoil mode shape is solved along each strip by the method of section 2.12.

Numerical integration of the unsteady pressures along the airfoil surface is used to calculate the modal unsteady aerodynamic force vector  $\{R\}_j$  due to the  $j^{\text{th}}$  natural mode. The  $j^{\text{th}}$  column of the modal aerodynamic matrix  $[A]$  is evaluated in a loop over all the modes as  $A_{ij} = \{\phi\}_i^T \{R\}_j$ . This procedure is followed for all of the blade natural modes to completely determine the  $[A]$  matrix.

### 3.2 SSME HPOTP Turbine Description

The method outlined above was used for the aeroelastic stability analysis of the Space Shuttle Main Engine (SSME) turbopump power turbine. The

SSME is a hydrogen-fueled liquid rocket engine which generates 512,000 lbf of thrust at full power. Each rocket engine is fed by four turbopumps, two high pressure and two low pressure booster pumps. The high pressure turbopumps are driven by axial-flow gas turbines which are powered by hydrogen-rich steam generated in individual preburners.

The High Pressure Fuel TurboPump (HPFTP) supplies the liquid hydrogen propellant to the main combustion chamber. The power turbine for the HPFTP generates 75,000 horsepower at a rotor speed of 36,000 RPM. Each turbine blade of this rotor transmits over 700 horsepower. The High Pressure Oxidizer TurboPump (HPOTP) supplies the oxidizer to the combustion chamber. The HPOTP gas turbine generates 30,000 horsepower at 28,000 RPM with each blade transferring approximately 300 horsepower.

Both the HPFTP and the smaller HPOTP operate in a severe environment at pressures of up to 5000 psi and temperatures close to 1600 deg F. Turbine blade cracking has been a continual problem for both of the high pressure turbopumps. A material replacement of single-crystal alloys for the HPFTP has effectively reduced the blade cracking problem.

A cross-sectional view of the HPOTP turbopump is provided on figure 9 which shows the pump impellers, shaft, gas turbine, preburner, and the turbine blade coolant jet ring. The first stage turbine blade has experienced frequent cracking in the shank region of the blade. The cracking is believed to be due to a resonant excitation of the second vibrational mode of the blade with cooling jets which direct a steam mixture to the blade shanks. There are 19 equally spaced cooling jets distributed circumferentially at a radius on the shank just above the top fir-tree attachment lobe. The blade dimensions are approximately 1.4 in. (3.56 cm) tall, tip chord of 0.66 in. (1.68 cm) and an airfoil span of 0.5 in. (1.27 cm) with a tip diameter of 10.8 in. (27.43 cm).

The HPOTP first stage turbine has blade-to-blade friction dampers installed to provide additional mechanical damping to keep vibrational amplitudes low. The original friction dampers were a one-piece design which did not provide sufficient damping to prevent fatigue cracking early in the development program. A redesign of the dampers in 1985 led to a reduction in cracking and longer service life, but the desired design life of 55 launches has yet to be realized.

NASA LeRC's involvement in the SSME HPOTP blade cracking problem was to assist in identifying methods for determining the level of mechan-

ical and aerodynamic damping which exist on the HPOTP turbine blade and to estimate the vibratory stress levels caused by the cooling jet and the blade-row aerodynamic interaction forcing functions. The aerodynamic damping for these blades is essentially due to the motion-dependent unsteady aerodynamic response of the fluid as the blade undergoes various modes of vibration. This report presents the aeroelastic stability analysis for the HPOTP turbine blade, including estimates of the level of aerodynamic damping, and a determination of the stability of the motion.

### 3.3 Aeroelastic Model

The aeroelastic model for the HPOTP first stage turbine blade consists of (a) the finite element model of the blade and (b) the aerodynamic strip definitions along the airfoil of the blade. The finite element model used for this work was provided by the the SSME contractor, Rocketdyne Division of Rockwell International Corp. The original finite element model was from the ANSYS general-purpose finite element program, and the model was converted into MSC/NASTRAN form for analysis at NASA LeRC.

The finite element model is three-dimensional, consisting of 10,014 nodal points and 7758 solid hexahedron elements as shown on figure 10. The turbine blade has extensions for the blade-to-blade friction dampers lo-

cated on the sides of the blade, between the top firtree lobe and the blade platform. This blade has a hollow core, to reduce the blade mass and thermal inertia and a tip seal to prevent spanwise flows over the tip of the blade.

Six aeroelastic strips, which represent approximate streamsurfaces, are defined along the span of the airfoil, from the blade platform to the tip shroud. These strips coincide with sections of the finite element model which have constant radii for the nodal points. The strips are indicated on figure 11, and a table of the cascade properties for each of the strips is included as Table I.

A plot showing the airfoil cross-section of the HPOTP turbine is included on figure 12, along with a table of airfoil coordinates. This turbine blade has blunt, rounded leading and trailing edges. The maximum airfoil thickness is approximately 30 percent of the airfoil chord length. The turbine turns the relative flow into the blade through up to 130 degrees.

### 3.4 Structural Dynamic Results

The MSC/NASTRAN finite element program was used to calculate the in-vacuum blade natural frequencies and modes. Springs were applied at the eight load bearing surfaces of the fir-tree lobes to simulate disk flexibility. The spring constants for these springs were determined by matching the first three calculated natural frequencies with those measured by Rocketdyne during high-speed rotating rig dynamic testing.

The effect of rotational speed was incorporated within the analysis by adding centrifugal loading and a temperature variation along the span of the blade. The temperature distribution for several operating speeds was estimated based upon flow path gas temperature measurements obtained during actual engine operation. The thermal variation of the blade material properties, for the directionally solidified alloy MAR-M-246, was modeled using a tabular description of the orthotropic material constants versus temperature.

The natural frequencies were calculated by performing a geometric non-linear static analysis (MSC/NASTRAN solution sequence 64) to simulate blade rotation and thermal loading. The differential stiffness matrix from the static solution was stored in a database file. The normal modes anal-

ysis (MSC/NASTRAN solution sequence 63) was performed by including the differential stiffness matrix within the linear global stiffness matrix. This method of accounting for the effect of centrifugal and other combined loadings on the normal modes of rotating structures is described by Lawrence, et. al. [42].

The first four natural frequencies of the blade were calculated at pump rotational speeds of 0, 19,500 and 28,000 RPM, speeds representative of typical power levels for an actual shuttle launch. A Campbell diagram is included as figure 13 which shows the variation of the natural frequencies with increasing pump speed. This blade shows only a very weak dependence of frequencies on the rotational speed. The effect of rotational speed on the frequency is due to centrifugal stiffening of the blade and thermal softening caused by increased temperature gradients. This blade, as is the case for most turbines, indicates that the thermal softening effect outweighs the stiffening effect which results in lower frequencies for higher rotational speeds.

The mode shapes from the analysis were normalized to give a unit generalized mass for each mode. Mode shapes orthogonalized in this manner are referred to as normal modes. Table II shows the calculated natural frequencies for the three rotor speeds.

Plots showing the deformed blade mode shapes for these natural frequencies at 28,000 RPM are shown on figures 14 and 15. These modes can be classified using common plate theory modes as modes (1) first bending, (2) first edgewise, (3) first torsion and (4) second bending. The occurrence of the edgewise mode as the second weakest mode is unusual for turbomachinery.

Plots of the mode shapes for strip no. 1, the strip closest to the blade tip are also shown on figure 16 as cross-sections through the blade airfoil section. These plots indicate that the first three modes are essentially rigid bending modes, with no appreciable chordwise bending of the airfoil. The fourth mode does display considerable bending of the airfoil section. These mode shapes displayed for this strip are the airfoil displacement descriptions which are enforced for each strip during the unsteady aerodynamic analysis.

### 3.5 Aerodynamic Results

The aerodynamic analysis for this blade was conducted for the 109% Rated Power Level (RPL) of the turbopump. This power level corresponds to a rotor speed of approximately 28,000 RPM. The SSME operates at this

power level for approximately 90% of the flight time, so the aeroelastic analysis is only presented for this rotor speed.

The velocity triangles along the span of the blade were constructed based on information supplied by Rocketdyne. The turbine operates within a fully subsonic flow regime where the velocities represent a blade tip Mach number of 0.24 with a relative inlet Mach number of around 0.30. The working fluid is hydrogen-rich superheated steam, and it was assumed to obey the perfect gas law having a ratio of specific heats of  $\gamma = 1.366$ . Velocity triangles for strip no. 1 showing the inlet and exit flows is included on figure 17. The superheated steam mixture has a sonic velocity at the turbine inlet of approximately  $a = 5600$  ft/sec and the inlet total pressure is  $P_1 = 4600$  psi.

The aeroelastic model for this turbine used the six strips indicated on figure 11, with the cascade properties used for each strip tabulated in table I. The steady potential flowfield was calculated for the strips separately and the computational grids and solutions stored in database files for use during the unsteady flow analysis. The computational grids used for the steady flow analysis consisted of a 78 x 25 mesh for the blade-to-blade global H-grid. A 70 x 11 C-grid was used for the local analysis grid, as described in section 2.11.

### 3.51 Steady Aerodynamic Results

Contour plots showing the steady Mach number variation within the flow field for strips no. 1 and 3 are included as figures 18 and 19. The plots show the large expansion of the flow and acceleration around the suction surface of the blade, near the LE. The two plots are presented with the same contour level ranges, and very little variation in the steady flow field is seen between these two strips.

Figure 20 shows the Mach number distributions along the surface of the airfoil. The figure includes the results for all six strips along the span of the airfoil. The large steady aerodynamic loading is evident for this turbine with the largest flow expansion near the leading edge of the suction surface. A similar figure indicating the airfoil steady surface pressure normalized by the inlet total pressure  $P_T$ , is on figure 21. The surface pressures imply that the largest steady aerodynamic loading along the airfoil is in the outer 40 percent region of the airfoil near the tip.

Inspection of the steady aerodynamic results in figures 20 and 21 shows that this turbine provides very little expansion and low increases in Mach

number from upstream to downstream, especially in comparison to aircraft gas turbines. The reason for this is that the dynamic pressure entering the blade is very high, approximately 480 psi at the tip. In addition, the inlet total pressure is close to 4600 psi, so that the static pressure nondimensionalized by total pressure can be misleading. The pressure difference across the airfoil can be up to 300 psi near the blade tip. These high pressures are a result of the superheated steam mixture having a high density and the high kinematic fluid velocities.

### 3.52 Unsteady Aerodynamic Results

The unsteady potential flows were calculated using the airfoil mode shapes from the finite element normal modes applied along each strip of the blade. At each strip, the flow reduced frequency parameter  $k$  was calculated based on the inlet relative flow velocity, strip airfoil chord length  $c$  and the assumed flutter frequency  $\omega_f$ . The interpolated airfoil mode shape was used to prescribe the direction of airfoil oscillation as discussed in section 3.1. The unsteady aerodynamic program was used to determine the unsteady potential solution and unsteady harmonic pressures caused by the prescribed aeroelastic conditions.

The harmonic unsteady pressures resulting from blade motion do not respond in-phase with the blade oscillation. The phase lag or lead of the pressure is an important parameter which governs the stability of the blade. Unsteady pressure is represented as a complex quantity, with the real part representing the pressure which is in-phase and the imaginary part representing the pressure which is 90 degrees out-of-phase with the blade motion.

The unsteady pressure distribution (real part) due to motion in the second mode, the edgewise mode, is shown along the blade span on figure 22. The ordinate is plotted as the unsteady pressure coefficient  $\tilde{C}_p$  multiplied by the square root of the generalized mass for the mode. The in-phase pressure response varies strongly along the airfoil span, with the largest pressure gradients within about 30 percent of the leading edge. Note that the pressures are somewhat irregular, especially near the leading edge. This might be due to the discrete description of the airfoil shape. This apparent dependence upon airfoil description is a common problem among both steady potential and unsteady potential flow CFD analysis.

The pressure distribution (imaginary part) for the same edgewise mode of motion is included in figure 23. The variation of the out-of-phase pressures, from the airfoil hub to the tip, obeys the same characteristics as the

real pressures, although these pressures are much smoother. A large change in the shape of the pressure distribution is seen between the last two strips along the blade span.

For a single mode of motion, the stability of the unsteady flow can be determined by inspecting the ratio of the real to the imaginary pressures at a particular location on the airfoil. If the pressures lag the blade motion, the motion is stable, if the pressures lead the motion it could become unstable. For systems which exhibit coupling between modes, this simple rule can no longer be used solely for determination of stability. An aerodynamic work parameter (Verdon [38]) is used to determine the unsteady aerodynamic energy transfer for arbitrary modes of airfoil motion. The aerodynamic work per cycle represents a measure of the aerodynamic work provided by the fluid during one complete cycle of airfoil motion. A condition when the aerodynamic work per cycle is negative implies that the airfoil is performing work on the fluid. Conversely, a positive work/cycle signifies that the fluid is doing work on the airfoil, which can lead to an instability of the airfoil oscillation.

Figure 24 shows the local work/cycle along the airfoil surface for the edgewise vibrational mode of the HPOTP. The work/cycle is unstable along almost the full chord length of the blade for all strips except the one

located at 58 percent of the airfoil span. These results would imply that the HPOTP turbine may be unstable in this edgewise mode of motion due to the motion-dependent response of the blade.

### 3.6 Aeroelastic Results

Calculations of the damped eigenvalues for the HPOTP first stage turbine were performed by solving the aeroelastic eigenvalue problem of equation (32). Four normal modes were retained within the modal analysis and the flutter analysis was performed when the assumed flutter frequency corresponded to the first three in-vacuum natural frequencies. The rotor was assumed to be tuned, and half of the total interblade phase angle modes were analyzed to reduce the computational time. The calculations were performed on the NASA LeRC Cray X-MP and Y-MP computer systems. The unsteady aerodynamic calculation, for a single strip and one interblade phase angle required approximately 12 CPU sec. The flutter analysis, for all strips at one interblade phase angle and one assumed frequency required 210 CPU secs.

The first stability analyses were performed when the effect of mechanical damping due to the friction dampers was neglected. Flutter was assumed to occur at frequencies close to each of the first three natural frequencies.

The eigenvalue problem of equation (32) was solved assuming four basis normal modes, whereas the system equations were of size  $4 \times 4$ . Each of the interblade phase angle modes was solved individually, so that the  $4 \times 4$  system was solved 39 times for vibration at an assumed frequency. The solution was accomplished by assuming a flutter frequency  $\omega_f$ , and the modal unsteady aerodynamic matrix was calculated followed by the eigensolution for the 4 eigenvalues. The aerodynamic damping for this turbine blade was extremely low, such that the damped natural frequency was nearly equal to the assumed frequency, therefore only one iteration was required for the flutter search.

The calculations showed that the HPOTP blade was aeroelastically stable for all interblade phase angles when the vibration occurred at frequencies close to the first and third natural frequencies. An inspection of the calculated modal eigenvectors showed that the aeroelastic modes were almost purely single-mode vibrations. The coupling due to the aerodynamic matrix  $[A]$  was not strong enough to cause any appreciable coupling in the modal space eigenvectors.

The aeroelastic eigenvalues  $\lambda$  are plotted as a function of the interblade phase angle  $\sigma$  in figure 25. This root locus is for the case when the vibration was at the first natural frequency,  $\omega_f = 4748$  Hz and the numbers

on this plot identify the different interblade phase angle modes for the rotor. Note that the eigenvalues are normalized by the assumed flutter frequency. Therefore the abscissa for this plot represents the system damping ratio and the ordinate represents the damped frequency ratio. The aerodynamic damping ratio for vibration at this mode varies from  $\zeta = 0.16$  percent of critical damping for  $\sigma = 350.77^\circ$  up to  $\zeta = 0.40$  percent for  $\sigma = 161.54^\circ$ . The results for vibration at the third normal mode resulted in lower damping ratios, although the rotor was stable for all phase angles (figure 26).

Calculations when the vibration was assumed to occur at the second normal mode, the edgewise mode, showed that the rotor was unstable for almost all the interblade phase angles considered. The root locus plot for this edgewise motion of the blade is included in figure 27. These results indicate that it is possible for this blade to undergo flutter in an edgewise mode of vibration when mechanical damping from the friction dampers is neglected. The only stable modes are for interblade phase angles in the range from 332.31 deg to 346.15 deg. This instability is surprising because the occurrence of flutter in an edgewise mode of vibration is rather uncommon. A combination of the high blade camber, large steady aerodynamic loading and flow expansion, and the edgewise mode of vibration appear to lead to this form of instability. This instability would not be

identified by the methods cited in the literature review because of the use of the simplified aerodynamic and blade dynamic models.

The potential for the HPOTP blades to experience flutter in this mode appears to explain the occurrence of blade shank cracking noticed during the SSME development program. In the early 1980's, blade-to-blade friction dampers were installed within the HPOTP rotor to attempt to damp out the unidentifiable vibrations. Continual high-cycle fatigue (HCF) cracking determined that a more efficient friction damper design was required. A new two-piece damper was incorporated in the HPOTP design which reduced the cracking problem significantly.

The mechanical damping provided by a blade-to-blade friction damper can be anywhere between 0.5 to 2.5 percent of critical damping (refs [43] and [44]). Measurements of the damper performance at Rocketdyne in a rotating dynamic test rig showed that the two-piece damper delivers almost 1 percent of critical damping when the blades are stimulated in the edgewise vibrational mode.

The stability calculations for the edgewise mode of vibration were continued when the effect of the friction dampers was included. This entailed adding modal damping of  $\zeta = 0.01$  for the edgewise mode of the blade.

The modal damping ratios for the three other modes were assumed to be zero. The eigensolution was performed for the 39 interblade phase angle modes and the resulting root locus is shown in figure 28. It is observed that including the effect of modal damping essentially translates the root locus to the left (more stable) and slightly lowers the root locus (lower frequency). These results indicate that the HPOTP rotor is fully stable when the effect of the turbine blade friction dampers is included. The increased positive mechanical damping completely overwhelms the unstable negative aerodynamic damping, resulting in the rotor becoming stable for all interblade phase angle modes.

This result agrees with the history of the SSME HPOTP rotor, where early in the development program, blade cracking could have been due to either (a) flutter or (b) large forced response due to very low aerodynamic damping. When additional mechanical damping was introduced by using a more effective friction damper, the blade cracking problem was reduced, a result in agreement with the analytical results presented here.

## CHAPTER 4 - CONCLUSION AND RECOMMENDATIONS

### 4.1 Conclusion

A modal aeroelastic analysis has been developed which has application to turbomachinery of general shape and over a range of flow regimes. The quasi-three-dimensional model combines the three-dimensional finite element modal results for the blade with stacked two-dimensional axisymmetric streamsurfaces along the span of the airfoil section of the blade. The steady flowfield along each strip was evaluated by solving for the nonlinear full potential flow using a finite-area solution method.

The unsteady flowfield due to airfoil oscillation was determined using a linearized unsteady potential flow model. The unsteady pressures were integrated along the airfoil surface for each strip to result in modal unsteady aerodynamic forces. A modal expansion of the unsteady forces was used to determine the aerodynamic matrix which couples the modes in modal space. An iterative complex eigenvalue problem was expressed in state-vector form to include the effect of modal damping.

This modal aeroelastic approach was applied to the flutter analysis of a high-energy turbine blade from a rocket engine oxidizer turbopump. Specific results of this analysis were:

- The natural frequencies for the turbine blade calculated using MSC/NASTRAN agreed very well with measurements reported by Rocketdyne. The modes occurred in the following order; (1) first bending, (2) first edgewise, (3) first torsion and (4) second bending.
- Steady-state aerodynamic results indicated that this turbine is subjected to high steady gas loading, with pressure differences across the airfoil of up to 300 psi. The axial pressure drop through the blade-row from upstream to downstream was much smaller.
- Unsteady aerodynamic results showed that the vibration of the blade at a single uncoupled mode, the first edgewise mode, would be unstable because the fluid supplies energy to the oscillation which results in a positive work of the fluid on the blade.
- Modal flutter calculations determined that the tuned rotor was stable for vibration of the rotor at either the first or the third natural frequency, for all of the tuned interblade phase angle modes of the rotor.

- Results from the flutter computation for vibration at the second natural frequency indicated that flutter would occur for almost all of the interblade phase angle modes of the rotor. This result agrees with the high-cycle fatigue cracking problem encountered during SSME development in the early 1980's.
- The addition of mechanical damping to simulate the blade friction dampers resulted in a stabilization of the self-excited vibration at the second natural frequency.

#### 4.2 Recommendations

Further expansion of this model could include emphasis on the development of advanced unsteady aerodynamic models. In particular, models based on linearizations of rotational flows, i.e. linearized Euler solution, with emphasis on three-dimensional geometries is planned. The addition of a three-dimensional aerodynamic model will simplify the logistical problems associated with the aeroelastic strips and the modal aerodynamic force computation. The advantage of a linearization of the unsteady Euler equations is that unsteady flows containing shocks and rotational flows can be analyzed where the potential equation is no longer valid. In

addition, the computational cost of the linearized Euler solution is not prohibitive, although it is significantly larger than for the linearized potential solution. An example of an unsteady linearized Euler solution for two-dimensional turbomachinery flows was presented by Hall and Crawley [45].

An effort is currently underway to analyze rotors which have small differences in natural frequencies of the blades within the rotor, the so-called mistuned aeroelastic model. The mistuned rotor model is a more practical representation of real-world turbomachinery since it takes into account the statistical differences in properties around the rotor. The occurrence of localized modes, where only a few blades respond with large amplitudes, can be captured using mistuning analyses. Blade failures typically occur with only a few blades cracking or fracturing, where these blades are referred to as "rogue" blade failures. A mistuned rotor analysis can provide better prediction of which blades may fail on a rotor due to flutter or forced response problems.

Finally, a more accurate representation of the friction-damper model, incorporating the micro-slip and macro-slip analyses could prove useful. The present method of accounting for friction-damping as equivalent modal damping is only a global representation of the effect of friction

dampers. Recent work has focused on applying nonlinear friction models using either lumped parameter or finite element and component mode models of blade elements. Some examples of the lumped parameter blade models using nonlinear friction damper elements are cited in References [44] and [46].

## REFERENCES

1. Carter, A.D., Kilpatrick, D.A., "Self-excited Vibration of Axial-flow Compressor Blades", Proceedings of the IME, Vol. 171, No. 7, pp 245-281, 1957
2. Jeffers, J.D., Meece, C.E., "F100 Fan Stall Flutter Problem Review and Solution", AIAA Journal of Aircraft, Vol. 12, No. 4, pp 350-357, 1975
3. Cardinale, V.M, Bankhead, H.R., McKay, R.A., "Experimental Verification of Turboblading Aeromechanics", Proceedings of AGARD 56th Symposium on Turbine Engine Testing, AGARD CP-293, 1980
4. Scalzo, A.J., Allen, J.M., Antos, R.J., "Analysis and Solution of a Non-Synchronous Vibration Problem in the Last Row Turbine Blade of a Large Industrial Combustion Turbine", ASME Paper 86-GT-230, 1986
5. Gabriel, F.K., Donato, V., "Telemetry Measurement of Combustion Turbine Blade Vibration in a High Temperature Environment", ASME Paper 86-GT-207, 1986
6. Mehmed, O., Kaza, K.R.V., Lubomski, J.F., Kielb, R.E., "Bending-Torsion Flutter of a Highly Swept Advanced Turboprop", NASA TM-82975, 1982
7. Mehmed, O., Kaza, K.R.V., "Experimental Classical Flutter Results of a Composite Advanced Turboprop Model", NASA TM-88792, 1986
8. Whitehead, D.S., "Force and Moment Coefficients for Vibrating Aerofoils in Cascade", ARC R&M 3254, 1960
9. Whitehead, D.S., "Bending Flutter of Unstalled Cascade Blades at Finite Deflection", ARC R&M 3386, 1962
10. Atassi, H., Akai, T.J., "Aerodynamic and Aeroelastic Characteristics of Oscillating Loaded Cascades at Low Mach Number Part 1: Pressure Distribution, Forces, and Moments", ASME Paper 79-GT-111, 1979
11. Smith, S.N., "Discrete Frequency Sound Generation in Axial Flow Turbomachines", ARC R&M 3709, 1972
12. Namba, M., "Subsonic Cascade Flutter with Finite Mean Lift", AIAA Journal, Vol. 13, No. 5, pp 586-593, 1975

13. Ni, R.H., "A Rational Analysis of Periodic Flow Perturbation in Supersonic Two-Dimensional Cascade", ASME Journal of Engineering for Power, Vol 101, pp 431-439, 1979
14. Verdon, J.M., "The Unsteady Aerodynamics of a Finite Supersonic Cascade with Subsonic Axial Flow", ASME Journal of Applied Mechanics, Vol. 40, No. 3, pp 667-671, 1973
15. Kurosaka, M., "On the Unsteady Supersonic Cascade With a Subsonic Leading Edge - An Exact First Order Theory Parts 1 and 2", ASME Journal of Engineering for Power, Vol. 96, No. 1, pp 13-31, 1974
16. Verdon, J.M., McCune, J.E., "Unsteady Supersonic Cascade in Subsonic Axial Flow", AIAA Journal, Vol. 13, No. 2, pp 193-201, 1975
17. Adamczyk, J.J., Goldstein, M.E., "Unsteady Flow in a Supersonic Cascade with Subsonic Leading-Edge Locus", AIAA Journal, Vol. 16, No. 12, pp 1248-1254, 1978
18. Miles, J.W., "The Compressible Flow Past an Oscillating Airfoil in a Wind Tunnel", Journal of the Aeronautical Sciences, Vol. 23, No. 7, 1956
19. Lane, F., "Supersonic Flow Past an Oscillating Cascade with Supersonic Leading-Edge Locus", Journal of the Aeronautical Sciences, Vol. 24, 1957
20. Ramsey, J.K., Kielb, R.E., "A Computer Program for Calculating Unsteady Aerodynamic Coefficients for Cascades in Supersonic Axial Flow", NASA TM-100204, 1987
21. Ni, R.H., Sisto, F., "Numerical Computation of Nonstationary Aerodynamics of Flat Plate Cascades in Compressible Flow", ASME Journal of Engineering for Power, Vol. 98, pp 165-170, 1976
22. Huff, D.L., Reddy, T.S.R., "Numerical Analysis of Supersonic Flow Through Oscillating Cascade Sections by Using a Deforming Grid", AIAA Paper 89-2805, 1989
23. Verdon, J.M., Caspar, J.R., "Subsonic Flow Past an Oscillating Cascade with Finite Mean Flow Deflection", AIAA Journal, Vol. 18, No. 5, pp 540-548, 1980

24. Verdon, J.M., Caspar, J.R., "A Linearized Unsteady Aerodynamic Analysis for Transonic Cascades", *Journal of Fluid Mechanics*, Vol. 149, pp 403-429, 1984
25. Whitehead, D.S., "The Calculation of Steady and Unsteady Transonic Flow in Cascades", Cambridge University Engineering Dept. Report CUED/A-Turbo/TR 118, 1982
26. Carta, F.O., "Coupled Blade-Disk-Shroud Flutter Instabilities in Turbojet Engine Rotors", *ASME Journal of Engineering for Power*, Vol. 89, pp 419-426, 1967
27. Snyder, L.E., Commerford, G.E., "Supersonic Unstalled Flutter in Fan Rotors; Analytical and Experimental Results", *ASME Journal of Engineering for Power*, pp 379-386, 1974
28. Mikolajczak, A.A., Arnoldi, R.A., Snyder, L.E., Stargardter, H., "Advances in Fan and Compressor Blade Flutter Analysis and Predictions", *AIAA Journal of Aircraft*, Vol. 12, No. 4, pp 325-332, 1975
29. Bendiksen, O.O., Friedmann, P., "Coupled Bending-Torsion Flutter in Cascades", *AIAA Journal*, Vol. 18, No. 2, 1980
30. Kaza, K.R.V., Kielb, R.E., "Flutter and Response of a Mistuned Cascade in Incompressible Flow", *AIAA Journal*, Vol. 20, No. 8, pp 1120-1127, 1982
31. Kielb, R.E., Kaza, K.R.V., "Aeroelastic Characteristics of a Cascade of Mistuned Blades in Subsonic and Supersonic Flows", *ASME Journal of Vibration, Acoustics, Stress and Reliability in Design*, Vol. 105, pp 425-433, 1983
32. Bendiksen, O.O., "Flutter of Mistuned Turbomachinery Rotors", *ASME Journal of Engineering for Gas Turbines and Power*, Vol. 106, pp 25-33, 1984
33. Crawley, E.F., Hall, K.C., "Optimization and Mechanisms of Mistuning in Cascades", *ASME Journal of Engineering for Gas Turbines and Power*, Vol. 107, pp 418-426, 1985
34. Kaza, K.R.V., Kielb, R.E., "Flutter of Turbofan Rotors with Mistuned Blades", *AIAA Journal*, Vol. 22, No. 11, pp 1618-1625, 1984

35. Kaza, K.R.V., Kielb, R.E., "Vibration and Flutter of Mistuned Bladed-Disk Assemblies", AIAA Journal of Propulsion and Power, Vol. 1, No. 5, pp 336-344, 1985
36. Turnberg, J., "Classical Flutter Stability of Swept Propellers", AIAA/ASME/ASCE/AHS 24th Structures, Structural Dynamics and Materials Conference, 83-0847-CP, May 2-4, 1983
37. Kaza, K.R.V., Mehmed, O., Narayanan, G.V., Murthy, D.V., "Analytical Flutter Investigation of a Composite Propfan Model", AIAA Journal of Aircraft, Vol. 26, No. 8, pp 772-780, 1989
38. Verdon, J.M., "Linearized Unsteady Aerodynamic Theory", Chapter II, AGARD Manual on Aeroelasticity in Axial Flow Turbomachines, Vol. 1, AGARD-AG-298, 1987
39. Caspar, J.R., Hobbs, D.E., Davis, R.L., "Calculation of Two-Dimensional Potential Cascade Flow Using Finite Area Methods", AIAA Journal, Vol. 18, No. 1, pp 103-109, 1980
40. Caspar, J.R., "Unconditionally Stable Calculation of Transonic Potential Flow Through Cascades Using an Adaptive Mesh for Shock Capture", ASME Paper 82-GT-238, 1982
41. Meirovitch, L., Analytical Methods in Vibrations, Macmillan Publishing Co., New York NY, 1967
42. Lawrence, C., Aiello, R.A., Ernst, M.A., McGee, O.G., "A NASTRAN Primer for the Analysis of Rotating Flexible Blades", NASA TM-89861, May 1987
43. Kielb, R.E., Griffin, H.H., Menq, C., "Evaluation of a Turbine Blade Damper Using an Integral Approach", AIAA Paper 88-2400, 1988
44. Sinha, A., Griffin, J.H., "Friction Damping of Flutter in Gas Turbine Engine Airfoils", AIAA Journal of Aircraft, Vol. 20, No. 4, 1983, pp 372-376
45. Hall, K.C., Crawley, E.F., "Calculation of Unsteady Flows in Turbomachinery using the Linearized Euler Equations", Presented at the Fourth Symposium on Unsteady Aerodynamics and Aeroelasticity of Turbomachines and Propellers, Aachen, West Germany, Sept 6-10, 1987

46. Sinha, A., Griffin, J.H., "Stability of Limit Cycles in Frictionally Damped and Aerodynamically Unstable Rotor Stages", *Journal of Sound and Vibration*, Vol 103, No. 3, 1985, pp 341-356

## APPENDIX A

### DERIVATION OF LINEARIZED UNSTEADY POTENTIAL EQUATION

The governing field equations for the flow of an inviscid, compressible fluid are described by the equations of mass, momentum, and energy conservation. These equations form the mathematical basis for description of the kinematic and thermodynamic modeling of fluid dynamics. The emphasis of the current work is to study the two dimensional, unsteady flow of an inviscid, compressible fluid. The equation set describing this flow is obtained by reducing the governing equations obtained from first principles.

The governing equations for the unsteady, compressible, inviscid flow of a fluid are equations (A.1) to (A.3).

$$\frac{\partial \rho}{\partial t} + \nabla \cdot (\rho \vec{V}) = 0 \quad (\text{A.1})$$

$$\frac{\partial \vec{V}}{\partial t} + \vec{V} \cdot \nabla \vec{V} = - \frac{1}{\rho} \nabla p \quad (\text{A.2})$$

$$\frac{\partial h}{\partial t} + \vec{V} \cdot \nabla h = \frac{\partial \rho}{\partial t} + \vec{V} \cdot \nabla p \quad (\text{A.3})$$

These equations are in conservation form and are general for a homogeneous fluid which is flowing without viscous dissipation, no heat addition, and no body forces.

The assumption that the fluid flows reversibly, and is thus isentropic, allows use of the perfect gas relationship which relates the local pressure to the density change as

$$\frac{p}{\rho^\gamma} = \text{Constant} \quad (\text{A.4})$$

The velocity potential is introduced by prescribing that the fluid flow is irrotational. This irrotationality condition is represented as

$$\nabla \times \vec{V} = 0 \quad (\text{A.5})$$

which permits defining the scalar velocity potential as

$$\vec{V} = \nabla \phi \quad (\text{A.6})$$

The equations (A.1-A.6) defined above represent the basis framework required for the development of the steady-state and the unsteady potential equations utilized within this work.

## UNSTEADY BERNOULLI-KELVIN THEOREM

A relationship which defines the dependence of the fluid properties with the kinematic state is now required. This formulation is obtained from the momentum equation of equation (A.2).

$$\frac{\partial \vec{V}}{\partial t} + \vec{V} \cdot \nabla \vec{V} = -\frac{1}{\rho} \nabla p$$

The following vector identity is useful for the reduction of this equation.

$$(\vec{V} \cdot \nabla) \vec{V} = \frac{1}{2} \nabla(\vec{V} \cdot \vec{V}) - \vec{V} \times (\nabla \times \vec{V}) \quad (\text{A.7})$$

Introduction of the irrotationality condition equation (A.5) and the velocity potential definition equation (A.6) reduces the above vector relationship to

$$(\vec{V} \cdot \nabla) \vec{V} = \frac{1}{2} \nabla(\nabla \phi \cdot \nabla \phi) \quad (\text{A.8})$$

Substitution of the above equation into the momentum equation (A.2), results in

$$\frac{\partial}{\partial t} (\nabla \phi) + \frac{1}{2} \nabla(\nabla \phi \cdot \nabla \phi) = -\frac{1}{\rho} \nabla p \quad (\text{A.9})$$

$$\nabla\phi_t + \nabla\left(\frac{(\nabla\phi\cdot\nabla\phi)}{2}\right) + \frac{1}{\rho}\nabla p = 0 \quad (\text{A.10})$$

Now, recalling from the calculus, since

$$\frac{1}{\rho}\nabla p = \nabla\left(\int\nabla\frac{p}{\rho}\right) \quad (\text{A.11})$$

substituting equation (A.11) results in the following integral equation

$$\nabla\phi_t + \nabla\left(\frac{(\nabla\phi\cdot\nabla\phi)}{2}\right) + \nabla\left(\int\nabla\frac{p}{\rho}\right) = 0 \quad (\text{A.12})$$

$$\nabla\left(\phi_t + \frac{(\nabla\phi\cdot\nabla\phi)}{2} + \int\nabla\frac{p}{\rho}\right) = 0$$

and integrating gives

$$\phi_t + \frac{(\nabla\phi\cdot\nabla\phi)}{2} + \int\nabla\frac{p}{\rho} = G(t) \quad (\text{A.13})$$

This equation is known as the Bernoulli-Kelvin equation and it applies along a streamline in the fluid.

## UNSTEADY FULL POTENTIAL EQUATION

The unsteady potential equation is derived by expansion and simplification of the mass conservation equation indicated in equation (A.1). This equation is reproduced below for completeness.

$$\frac{\partial \rho}{\partial t} + \nabla \cdot (\rho \vec{V}) = 0 \quad (\text{A.1})$$

The divergence term of this equation may be expanded and the equation rearranged to result in

$$\frac{1}{\rho} \frac{\partial \rho}{\partial t} + \nabla \cdot \vec{V} + \frac{1}{\rho} \vec{V} \cdot \nabla \rho = 0 \quad (\text{A.14})$$

The first term of this equation may be written as the product of two partial derivatives using the chain rule

$$\frac{1}{\rho} \frac{\partial \rho}{\partial t} = \frac{1}{\rho} \frac{\partial \rho}{\partial p} \frac{\partial p}{\partial t} \quad (\text{A.15})$$

and assuming the fluid behaves as a perfect gas, under isentropic conditions, the sonic velocity becomes

$$a^2 = \left( \frac{\partial p}{\partial \rho} \right)_{s = \text{constant}} \quad (\text{A.16})$$

such that equation (A.15) now becomes

$$\frac{1}{\rho} \frac{\partial \rho}{\partial t} = \frac{1}{\rho a^2} \frac{\partial p}{\partial t} \quad (\text{A.17})$$

A relationship for  $\frac{\partial p}{\partial t}$  is determined through the use of the Bernoulli-Kelvin Theorem of equation (A.13). Differentiating equation (A.13) with respect to time results in

$$\phi_{tt} + \frac{\partial}{\partial t} \left( \frac{\nabla \phi \cdot \nabla \phi}{2} \right) + \frac{\partial}{\partial t} \int \frac{\nabla \tilde{\phi}}{\rho} = 0 \quad (\text{A.18})$$

where the derivative of the time constant  $G(t)$  has arbitrarily been set to zero. The last term of equation (A.18) can be written as

$$\frac{\partial}{\partial t} \int \nabla \frac{p}{\rho} = \frac{1}{\rho} \frac{\partial p}{\partial t} \quad (\text{A.19})$$

and so rearranging equation (A.18) and substituting equation (A.19) gives

$$\frac{\partial p}{\partial t} = -\rho \left( \phi_{tt} + \frac{\partial}{\partial t} \left( \frac{\nabla \phi \cdot \nabla \phi}{2} \right) \right) \quad (\text{A.20})$$

and substituting equation (A.20) into equation (A.17) results in the following relation for the first term in equation (A.14)

$$\frac{1}{\rho} \frac{\partial \rho}{\partial t} = -\frac{1}{a^2} (\phi_{tt} + \nabla \phi \cdot \nabla \phi_t) \quad (\text{A.21})$$

The second term from equation (A.14) is simply the Laplacian of the potential

$$\nabla \cdot \vec{V} = \nabla^2 \phi \quad (\text{A.22})$$

The last term of equation (A.14) can be written as

$$\begin{aligned} \frac{\vec{V} \cdot \nabla \rho}{\rho} &= \frac{\nabla \phi \cdot \nabla \rho}{\rho a^2} \\ &= \frac{\nabla \phi \cdot \nabla}{a^2} \left( \int \nabla \frac{\rho}{\rho} \right) \end{aligned} \quad (\text{A.23})$$

and solving equation (A.12) for  $\nabla \left( \int \frac{\nabla \tilde{\phi}}{\rho} \right)$  and substituting into equation (A.22) gives

$$\frac{\vec{V} \cdot \nabla \rho}{\rho} = -\frac{\nabla \phi \cdot \nabla}{a^2} \left( \phi_t + \frac{\nabla \phi \cdot \nabla \phi}{2} \right) \quad (\text{A.24})$$

At this point, each of the individual terms from the continuity equation of equation (A.14) have been expanded. These terms of equation (A.21), (A.22), (A.24) are substituted back into equation (A.14).

$$\phi_{tt} + 2 \nabla \phi \cdot \nabla \phi_t + \frac{1}{2} \nabla \phi \cdot \nabla (\nabla \phi \cdot \nabla \phi) = a^2 \nabla^2 \phi \quad (\text{A.25})$$

This equation is known as the unsteady full potential equation. It contains only terms of the scalar velocity potential  $\phi$  and the local fluid sonic velocity  $a$ .

An expression for the sonic velocity can be obtained from the Bernoulli-Kelvin equation developed previously. Along a streamline, from a point at far upstream infinity where the flow is fully steady, the Bernoulli equation (A.13) becomes

$$a^2 = a_\infty^2 + (\gamma - 1) \left[ \frac{V_\infty^2}{2} - \phi_t - \frac{1}{2} (\nabla\phi \cdot \nabla\phi) \right] \quad (\text{A.26})$$

So the above equations (A.25) and (A.26) completely describe the unsteady potential flow for a compressible, inviscid fluid.

#### LINEARIZED POTENTIAL EQUATIONS

The time varying potential is assumed to be a series expansion in time of harmonic terms as shown below

$$\phi(x,y,t) = \Phi(x,y) + \tilde{\phi}(x,y)e^{i\omega t} + O(\varepsilon^2) \quad (\text{A.27})$$

where  $\varepsilon$  is of the order of the small perturbations  $\vec{r}$ , and  $\tilde{\phi}(x,y)$ . This assumption results in a zeroth-order term which represents the steady-state

potential  $\Phi(x,y)$ , and a first-order harmonic unsteady potential  $\tilde{\phi}(x,y,t)e^{i\omega t}$ . The terms of higher than first order in  $\varepsilon$ , i.e. higher than  $e^{i\omega t}$ , are truncated from the expansion. This expansion can now be substituted into the unsteady full potential equation (A.25).

The following expressions will be useful for this development. They are obtained by applying the expansion of equation (A.27).

$$\begin{aligned}
 \phi_{tt} &= -\omega^2 \tilde{\phi} \\
 \nabla \phi &= \nabla \Phi + \nabla \tilde{\phi} \\
 \nabla \phi_t &= i\omega \nabla \tilde{\phi} \\
 \nabla^2 \phi &= \nabla^2 \Phi + \nabla^2 \tilde{\phi} \\
 \nabla \phi \cdot \nabla \phi &= (\nabla \Phi)^2 + (\nabla \tilde{\phi})^2 + 2 \nabla \Phi \cdot \nabla \tilde{\phi}
 \end{aligned}
 \tag{A.28}$$

The above relations can be used to expand the unsteady full potential equation to result in an equation which contains terms of both  $O(0)$  and order  $O(\varepsilon)$ . These terms are grouped according to their order into two equations.

The equation consisting of terms of order  $O(0)$  is known as the steady full potential equation as shown below.

$$\frac{1}{2} \nabla \Phi \cdot \nabla (\nabla \Phi \cdot \nabla \Phi) = a^2 \nabla^2 \Phi
 \tag{A.29}$$

The same equation can be obtained by dropping the time-dependent terms from the unsteady full potential equation of equation (A.25).

An equivalent equation for the terms of order  $O(\varepsilon)$  is shown below

$$\begin{aligned} & -\omega^2 \tilde{\phi} + 2i\omega \nabla\Phi \cdot \nabla\tilde{\phi} + \frac{1}{2} \nabla\tilde{\phi} \cdot \nabla(\nabla\Phi)^2 + \nabla\Phi \cdot \nabla(\nabla\Phi \cdot \nabla\tilde{\phi}) \\ & + \nabla\tilde{\phi} \cdot \nabla(\nabla\Phi \cdot \nabla\tilde{\phi}) = a^2 \nabla^2 \tilde{\phi} \end{aligned} \quad (\text{A.30})$$

This equation represents the linearized unsteady potential equation, where the potential  $\phi(x,y)$  is assumed to be harmonic in time.

The substantial derivative operator for the potential having harmonic time dependence becomes

$$\frac{D\tilde{\phi}}{Dt} = i\omega\tilde{\phi} + \nabla\Phi \cdot \nabla\tilde{\phi}$$

$$\frac{D^2\tilde{\phi}}{Dt^2} = -\omega^2\tilde{\phi} + 2i\omega\nabla\Phi \cdot \nabla\tilde{\phi} + \nabla\Phi \cdot \nabla(\nabla\Phi \cdot \nabla\tilde{\phi})$$

The substitution of the above substantial derivative operators into the unsteady potential equation (A.30) simplifies to

$$\frac{D^2 \tilde{\phi}}{Dt^2} + \frac{1}{2} \nabla \tilde{\phi} \cdot \nabla (\nabla \Phi)^2 + \nabla \tilde{\phi} \cdot \nabla (\nabla \Phi \cdot \nabla \tilde{\phi}) = a^2 \nabla^2 \tilde{\phi} \quad (\text{A.31})$$

This equation represents the linearized unsteady potential flow where the unsteady potential  $\tilde{\phi}$  is assumed to be harmonic in time and of small amplitude.

Table I. HPOTP turbine aeroelastic strip properties

Strip Number	Percent Airfoil Span	Strip Height (% Span)	Cascade Solidity	Stagger Angle (deg)	Inlet Rel. Mach Number
1	76.0	33.0	1.565	30.0	0.268
2	58.0	17.0	1.572	28.3	0.266
3	42.0	15.0	1.582	26.8	0.264
4	28.0	13.0	1.600	26.4	0.263
5	16.0	10.0	1.608	25.4	0.262
6	8.0	12.0	1.613	24.6	0.261

Table II. HPOTP turbine calculated natural frequencies

Mode Number	NASTRAN Natural Frequencies (Hz)		
	Rotor Speed 0 RPM	Rotor Speed 19,000 RPM	Rotor Speed 28,000 RPM
1	4762	4759	4748
2	10,192	10,083	9950
3	17,251	16,945	16,580
4	24,635	24,158	23,682

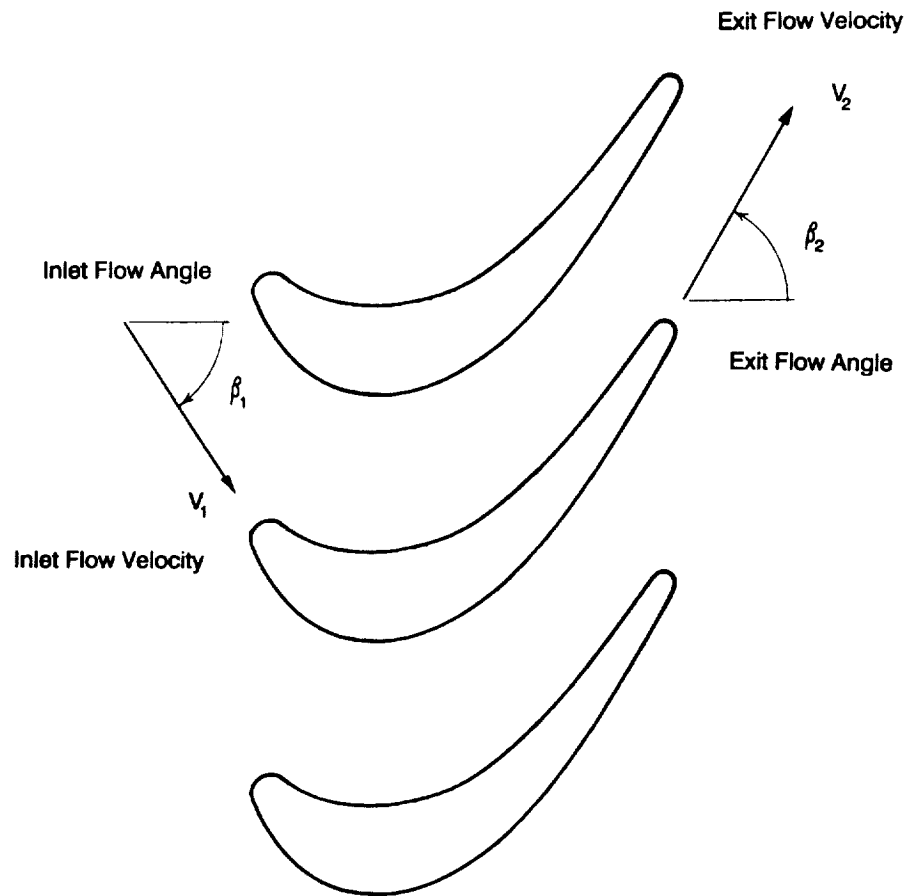


Figure 1. Cascade representation of rotor inlet and exit flows

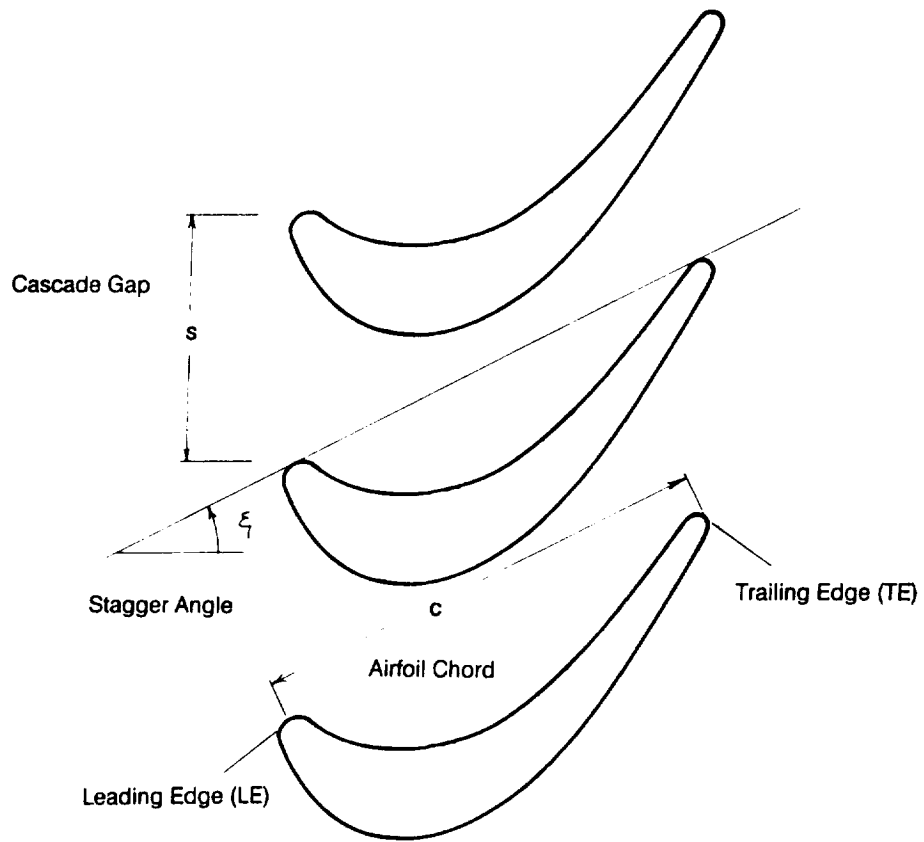


Figure 2. Cascade and airfoil geometry and nomenclature

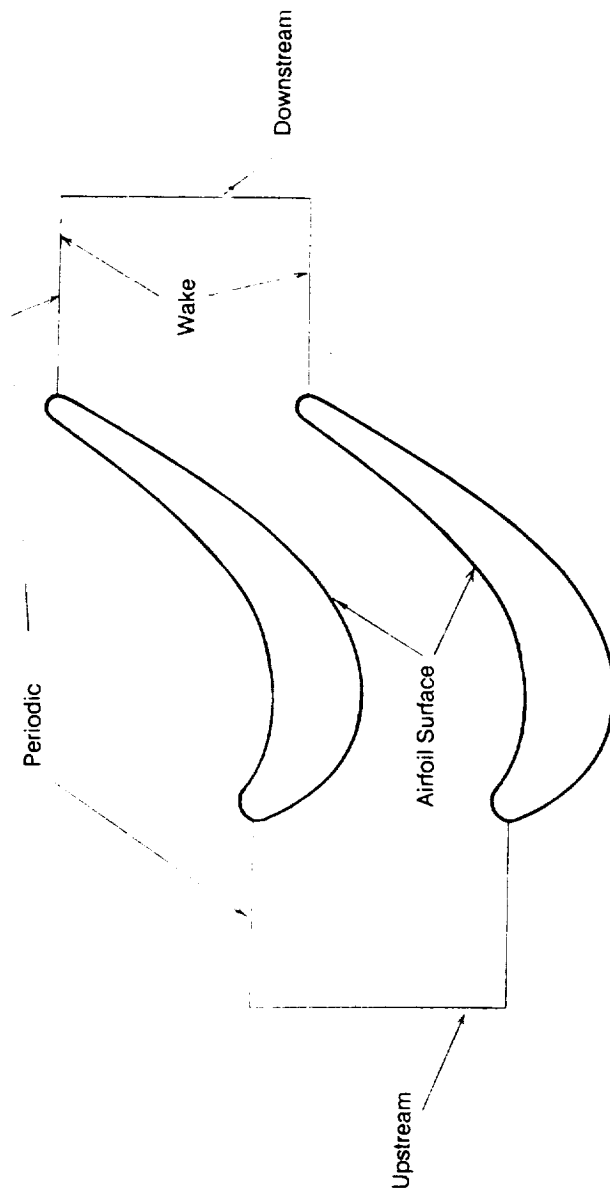
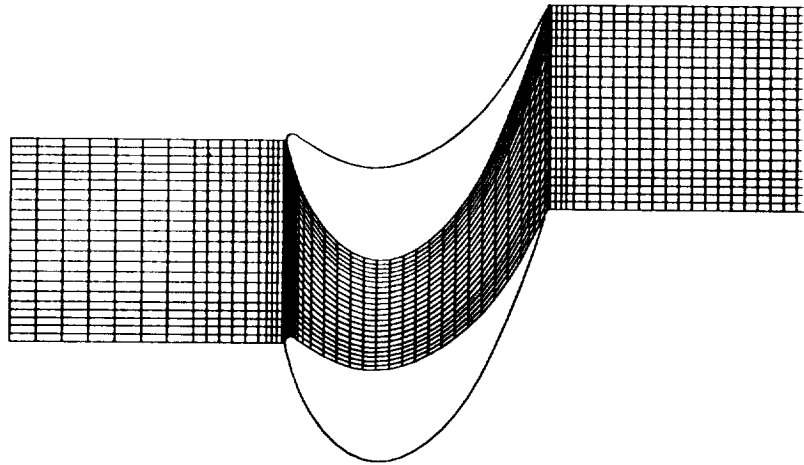
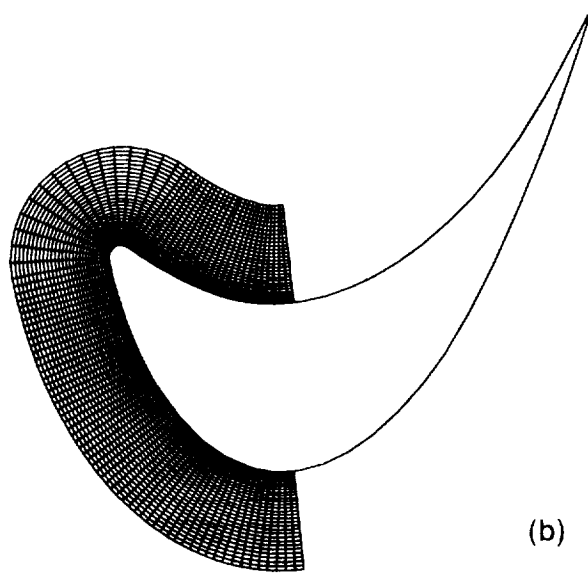


Figure 3. Steady solution blade-to-blade passage and boundary conditions



(a)



(b)

Figure 4. Steady flow computational meshes, (a) global mesh, (b) local mesh

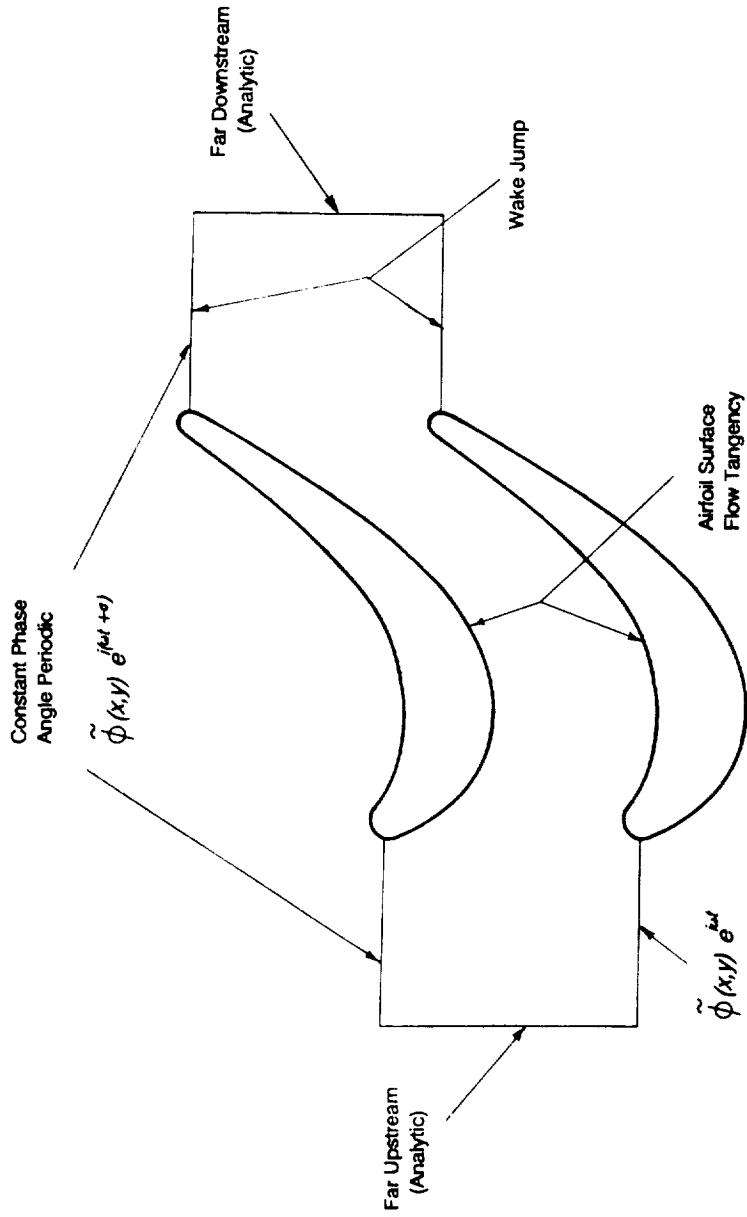


Figure 5. Unsteady solution cascade boundary conditions

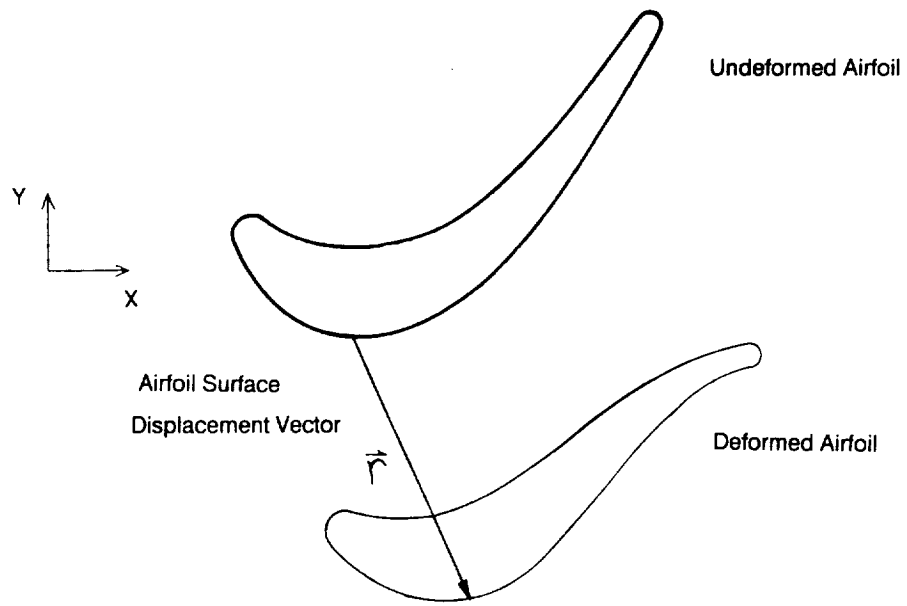


Figure 6. Oscillating airfoil displacement vector  $\vec{r}$  definition

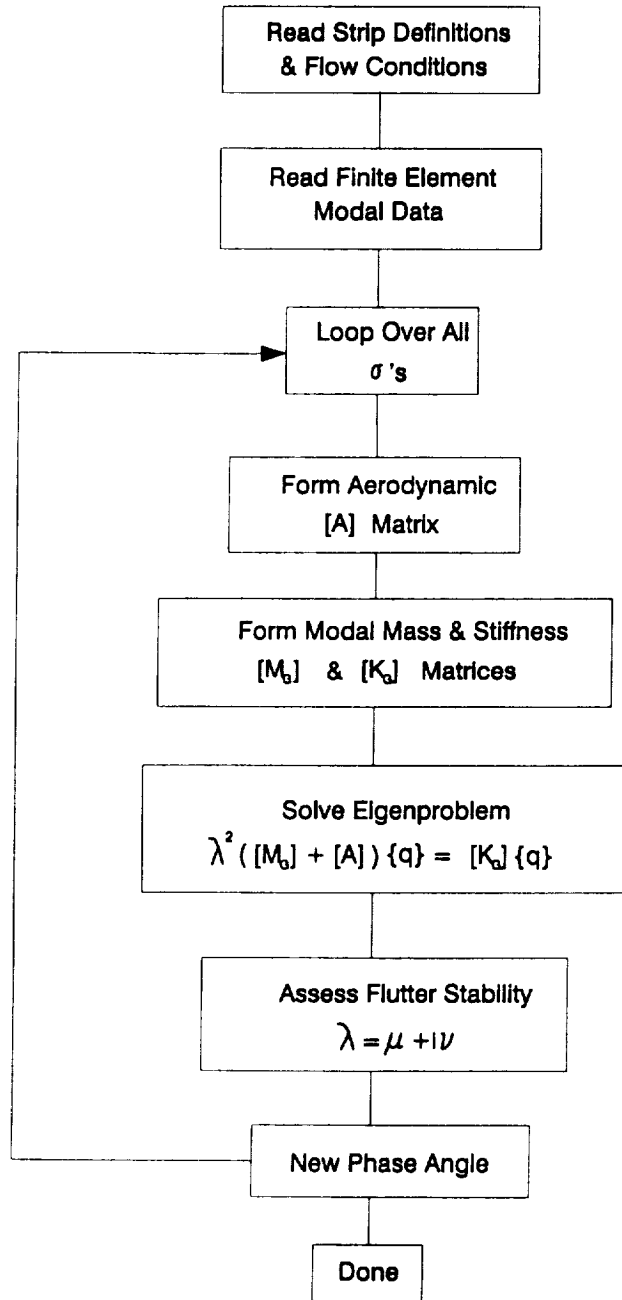


Figure 7. FREPS program aeroelastic stability logic flowchart

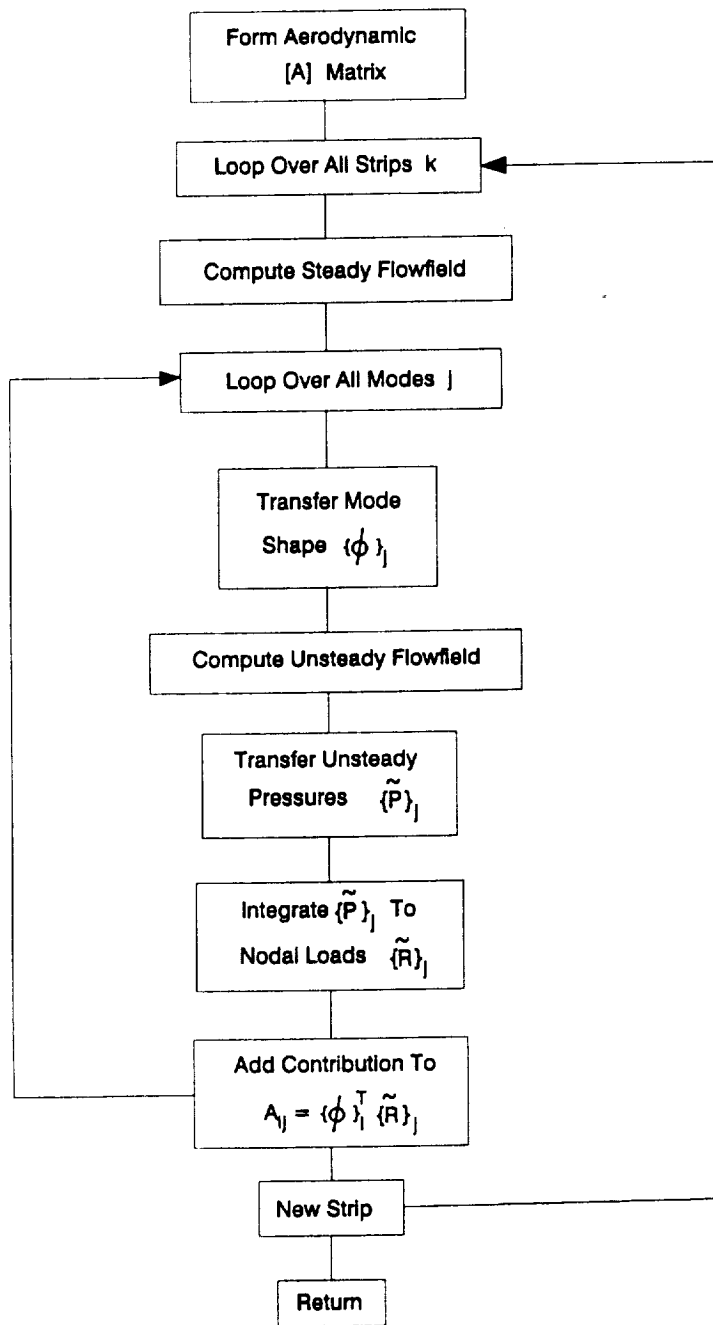


Figure 8. Modal aerodynamic matrix [A] logic flowchart

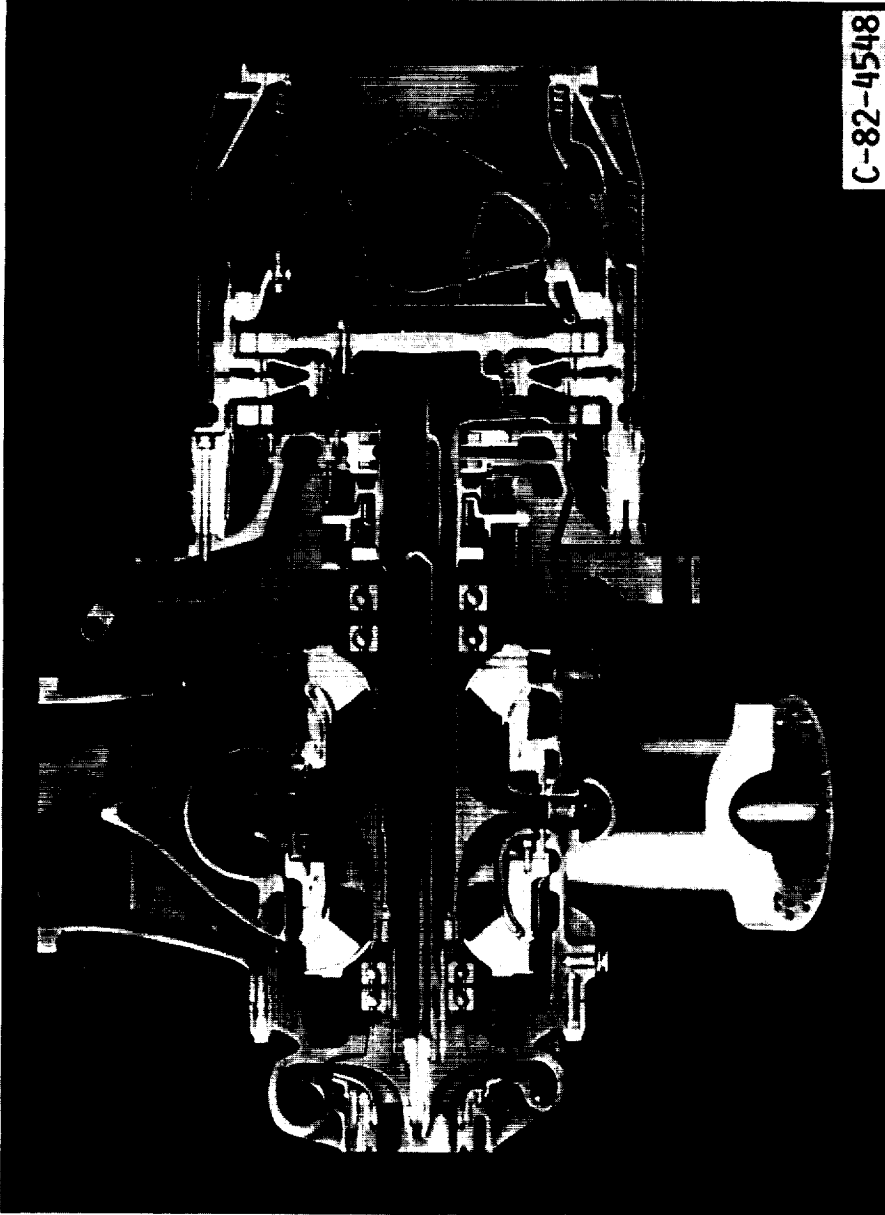
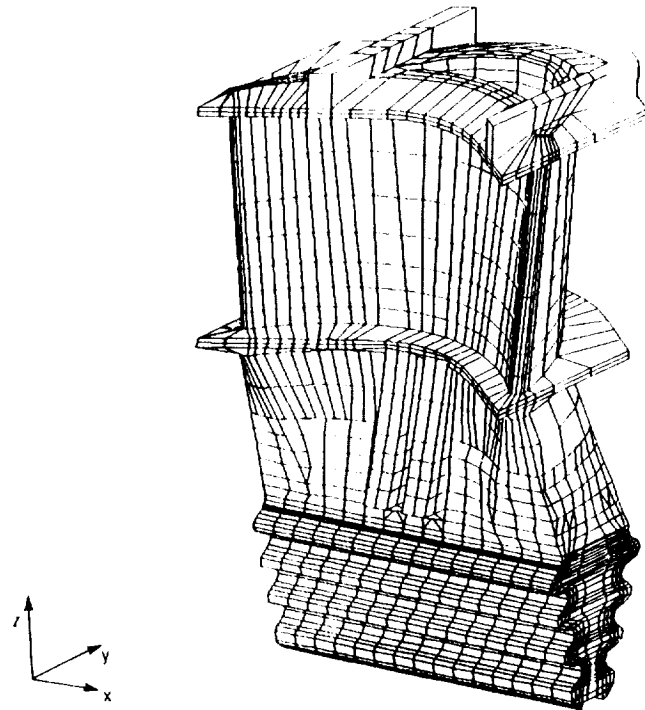


Figure 9. SSME high pressure oxygen turbopump (HPOTP) cross-section



**10,014 Node Points**

**7758 Brick Elements**

Figure 10. SSME HPOTP turbine blade finite element model

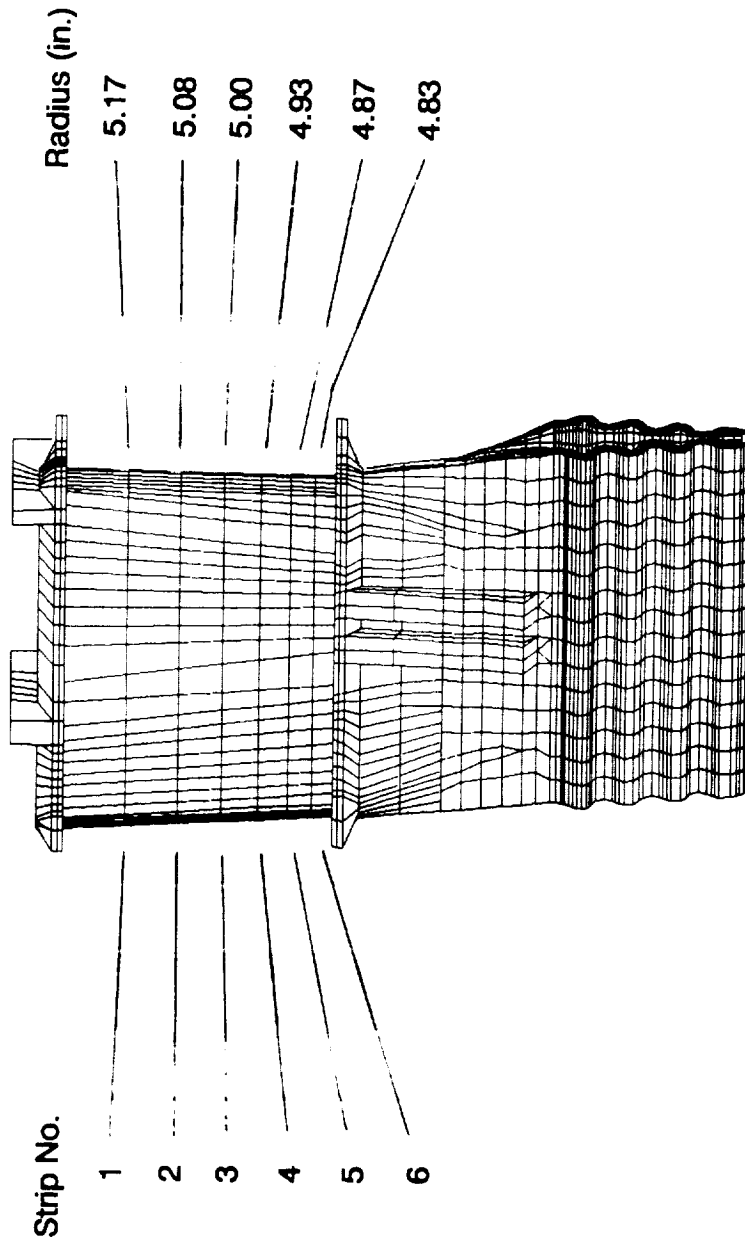


Figure 11. Turbine blade aeroelastic strip definitions

Pressure Surface		Suction Surface	
X	Y	X	Y
0.0000	0.0000	0.0000	0.0000
0.0085	0.0095	-0.0032	-0.0125
0.0206	0.0138	-0.0027	-0.0172
0.0328	0.0124	0.0145	-0.0767
0.0532	0.0003	0.0480	-0.1670
0.0829	-0.0179	0.0816	-0.2370
0.1128	-0.0346	0.1150	-0.2935
0.1427	-0.0501	0.1486	-0.3398
0.1725	-0.0640	0.1820	-0.3777
0.2024	-0.0764	0.2156	-0.4088
0.2323	-0.0868	0.2490	-0.4337
0.2621	-0.0953	0.2825	-0.4533
0.2920	-0.1016	0.3160	-0.4675
0.3219	-0.1058	0.3495	-0.4769
0.3517	-0.1075	0.3829	-0.4815
0.3816	-0.1066	0.4150	-0.4815
0.4115	-0.1031	0.4456	-0.4774
0.4413	-0.0971	0.4760	-0.4690
0.4712	-0.0884	0.5066	-0.4568
0.5056	-0.0769	0.5372	-0.4406
0.5400	-0.0625	0.5678	-0.4205
0.5746	-0.0453	0.5984	-0.3966
0.6091	-0.0254	0.6290	-0.3685
0.6437	-0.0023	0.6596	-0.3361
0.6781	0.0237	0.6900	-0.2993
0.7125	0.0532	0.7205	-0.2576
0.7471	0.0861	0.7511	-0.2106
0.7816	0.1227	0.7787	-0.1631
0.8162	0.1635	0.8031	-0.1158
0.8506	0.2089	0.8277	-0.0640
0.8852	0.2596	0.8521	-0.0080
0.9196	0.3166	0.8767	0.0520
0.9540	0.3813	0.9011	0.1157
0.9741	0.4212	0.9256	0.1832
0.9821	0.4255	0.9502	0.2541
0.9908	0.4247	0.9748	0.3286
0.9975	0.4190	0.9983	0.4063
1.0000	0.4108	0.9998	0.4085

Pressure Surface		Suction Surface	
X	Y	X	Y
0.0000	0.0000	0.0000	0.0000
0.0085	0.0095	-0.0032	-0.0125
0.0206	0.0138	-0.0027	-0.0172
0.0328	0.0124	0.0145	-0.0767
0.0532	0.0003	0.0480	-0.1670
0.0829	-0.0179	0.0816	-0.2370
0.1128	-0.0346	0.1150	-0.2935
0.1427	-0.0501	0.1486	-0.3398
0.1725	-0.0640	0.1820	-0.3777
0.2024	-0.0764	0.2156	-0.4088
0.2323	-0.0868	0.2490	-0.4337
0.2621	-0.0953	0.2825	-0.4533
0.2920	-0.1016	0.3160	-0.4675
0.3219	-0.1058	0.3495	-0.4769
0.3517	-0.1075	0.3829	-0.4815
0.3816	-0.1066	0.4150	-0.4815
0.4115	-0.1031	0.4456	-0.4774
0.4413	-0.0971	0.4760	-0.4690
0.4712	-0.0884	0.5066	-0.4568
0.5056	-0.0769	0.5372	-0.4406
0.5400	-0.0625	0.5678	-0.4205
0.5746	-0.0453	0.5984	-0.3966
0.6091	-0.0254	0.6290	-0.3685
0.6437	-0.0023	0.6596	-0.3361
0.6781	0.0237	0.6900	-0.2993
0.7125	0.0532	0.7205	-0.2576
0.7471	0.0861	0.7511	-0.2106
0.7816	0.1227	0.7787	-0.1631
0.8162	0.1635	0.8031	-0.1158
0.8506	0.2089	0.8277	-0.0640
0.8852	0.2596	0.8521	-0.0080
0.9196	0.3166	0.8767	0.0520
0.9540	0.3813	0.9011	0.1157
0.9741	0.4212	0.9256	0.1832
0.9821	0.4255	0.9502	0.2541
0.9908	0.4247	0.9748	0.3286
0.9975	0.4190	0.9983	0.4063
1.0000	0.4108	0.9998	0.4085

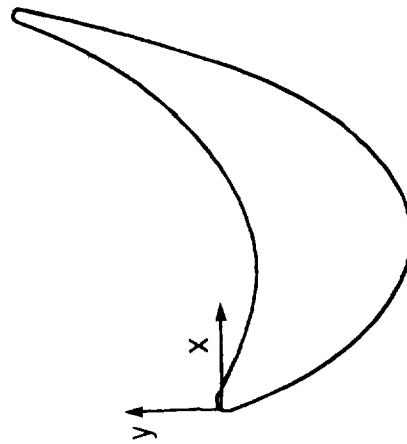


Figure 12. Turbine blade airfoil description at 75% span

*SSME High Pressure Oxidizer Turbopump Campbell Diagram  
First Stage Turbine Blade*

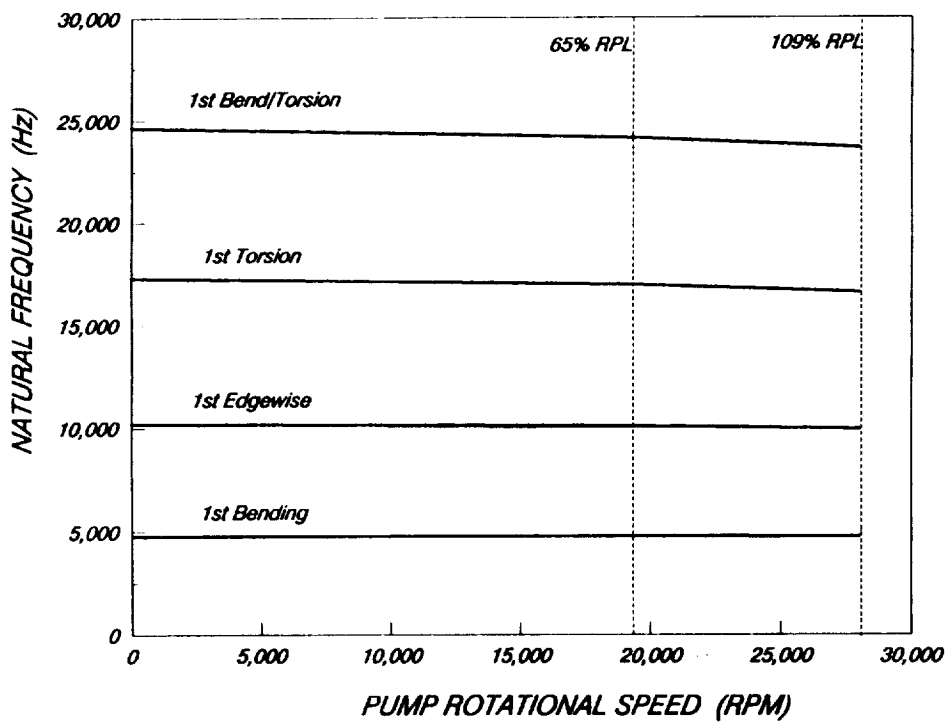
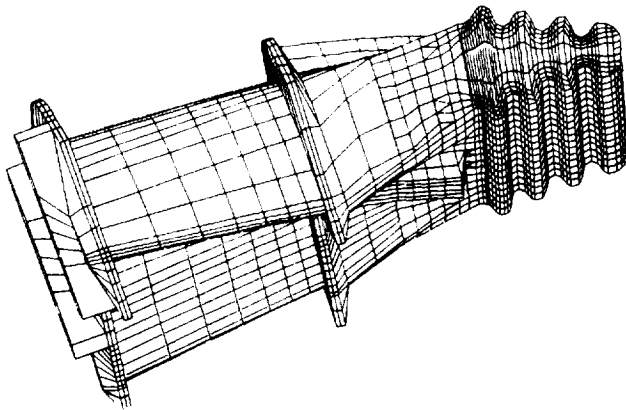
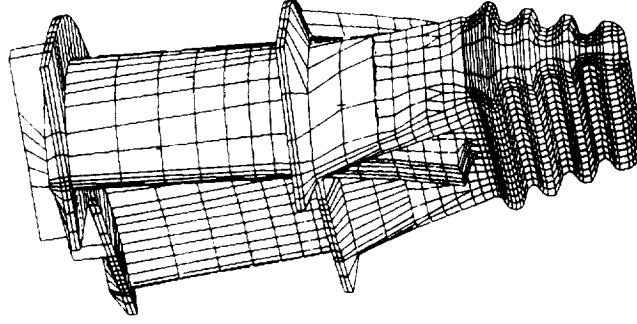


Figure 13. Calculated natural frequencies versus rotational speed

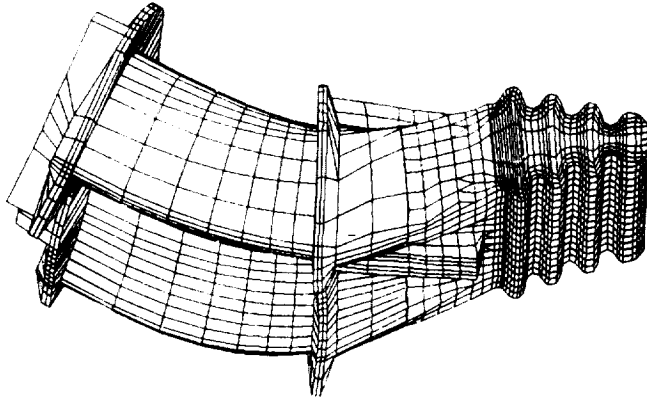


**Mode 1**  
**Frequency 4748 Hz**

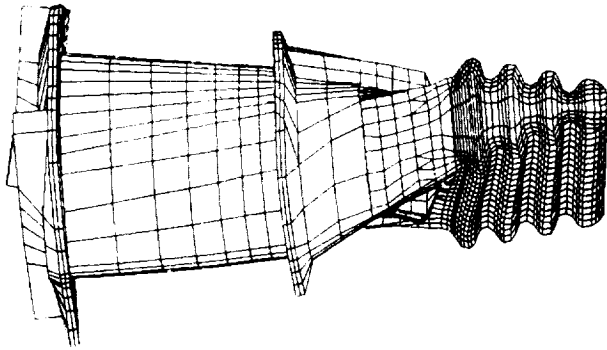


**Mode 2**  
**Frequency 9950 Hz**

Figure 14. Calculated deformed mode shapes for modes 1 and 2



**Mode 4**  
**Frequency 23,682 Hz**



**Mode 3**  
**Frequency 16,580 Hz**

Figure 15. Calculated deformed mode shapes for modes 3 and 4

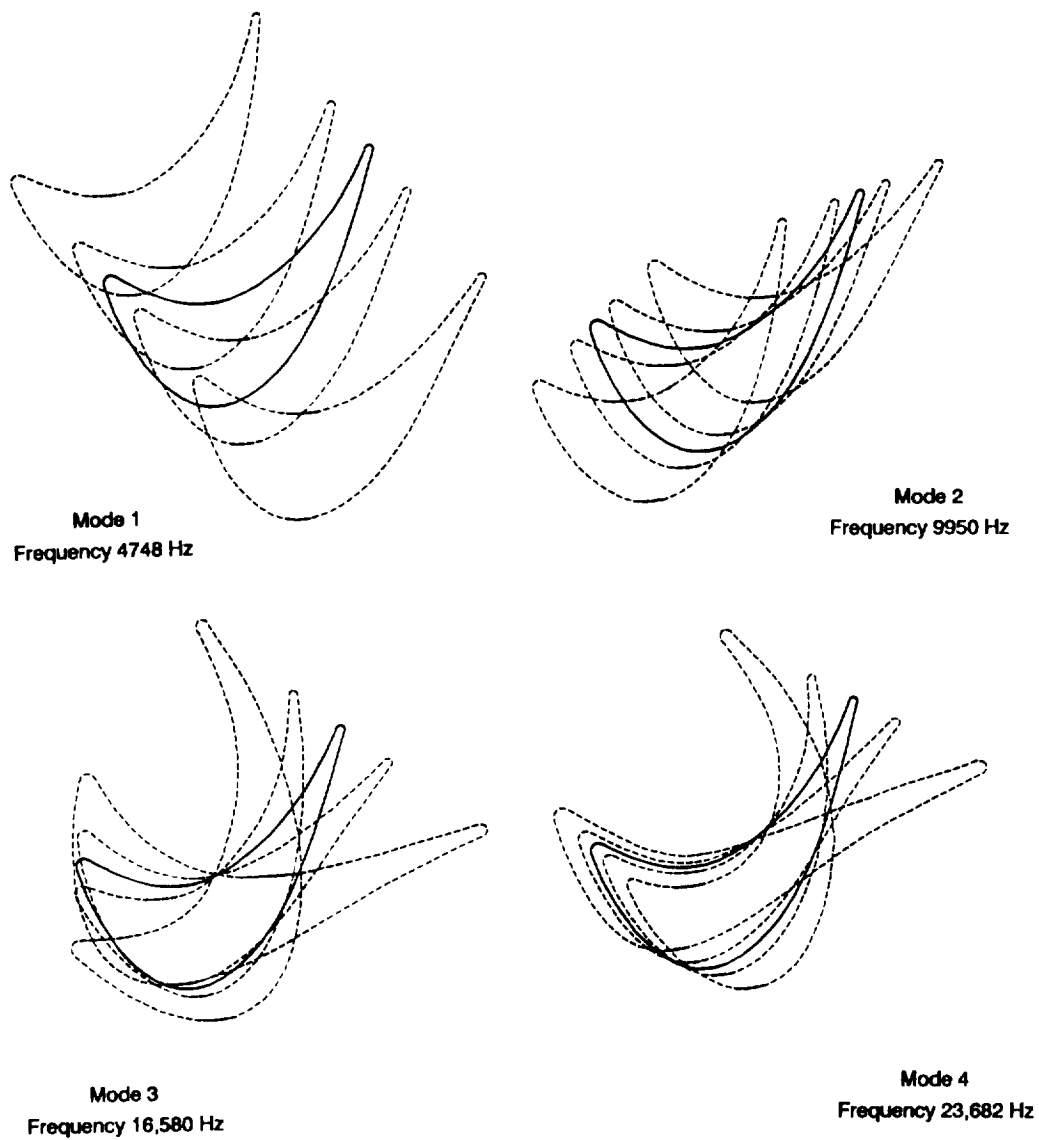
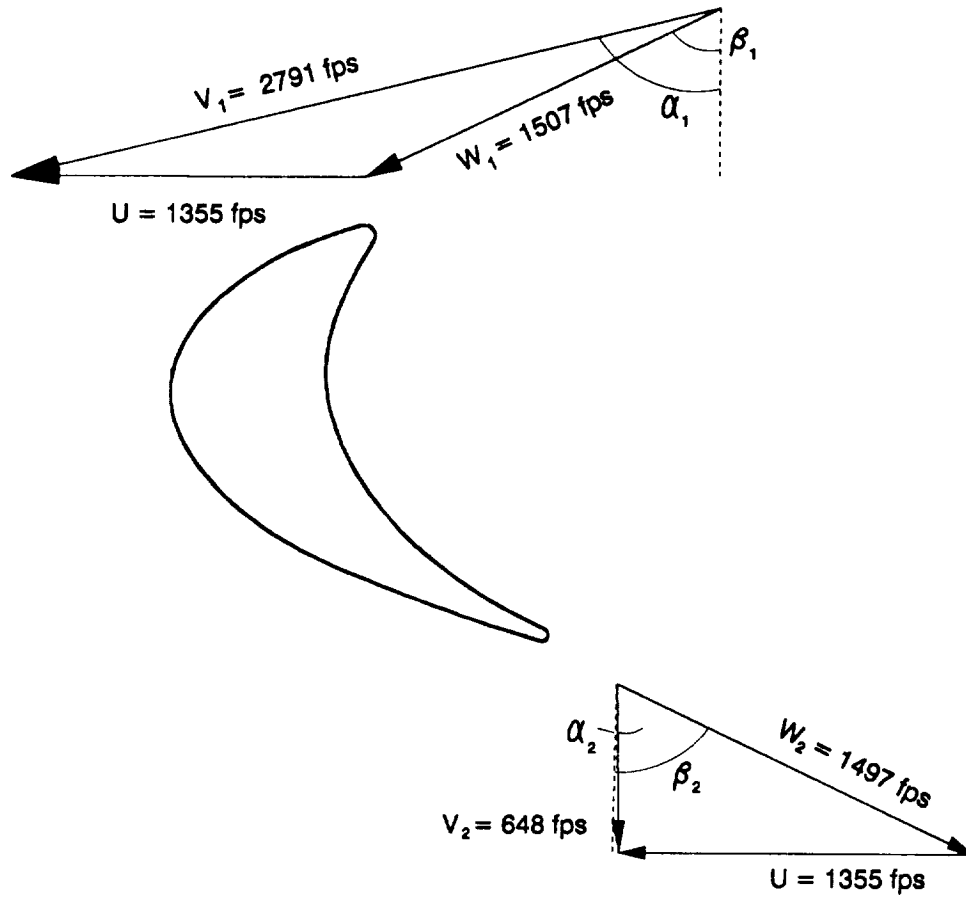


Figure 16. Airfoil mode shape cross-sections at strip no. 1

$$\alpha_1 = 76.6 \text{ Deg}$$

$$\beta_1 = 64.5 \text{ Deg}$$



$$\alpha_2 = 0.5 \text{ Deg}$$

$$\beta_2 = 64.3 \text{ Deg}$$

Figure 17. Turbine blade fluid velocity diagram at strip no. 1

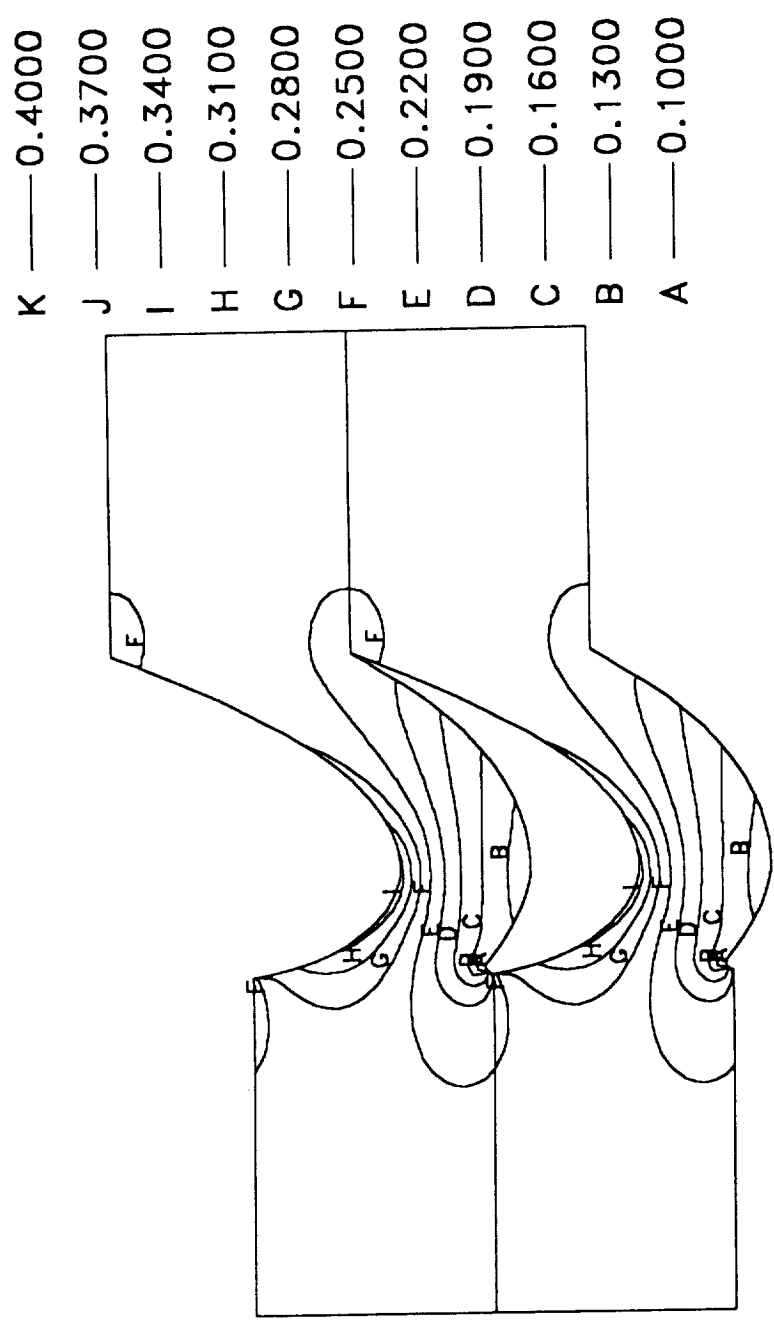


Figure 18. Steady flow Mach number contours for strip no. 1

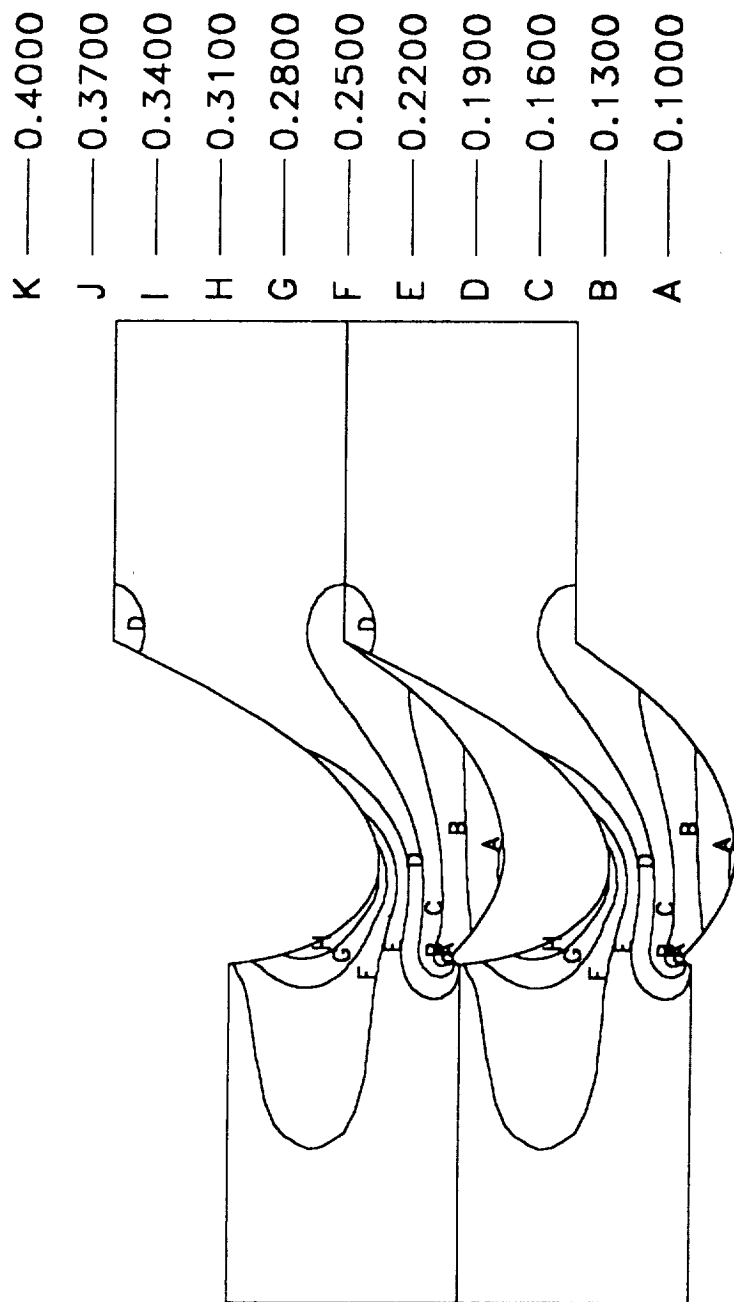


Figure 19. Steady flow Mach number contours for strip no. 3

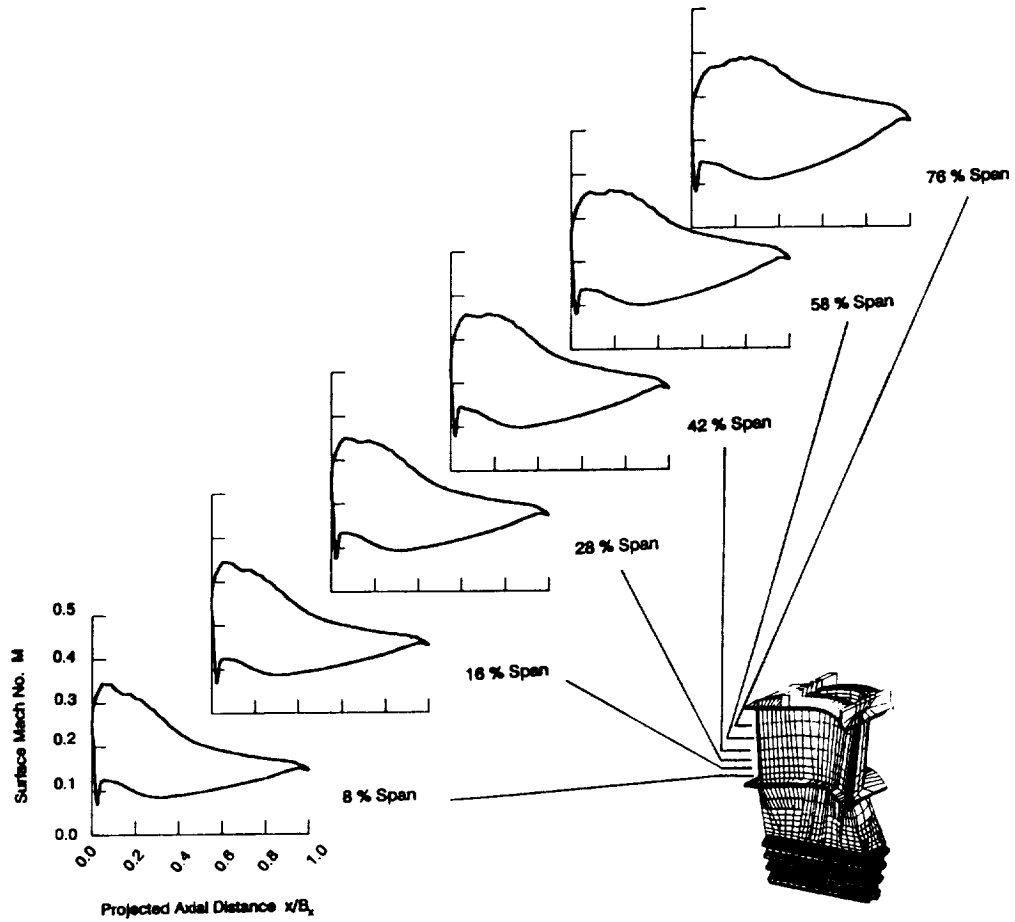


Figure 20. Turbine blade surface Mach number distributions

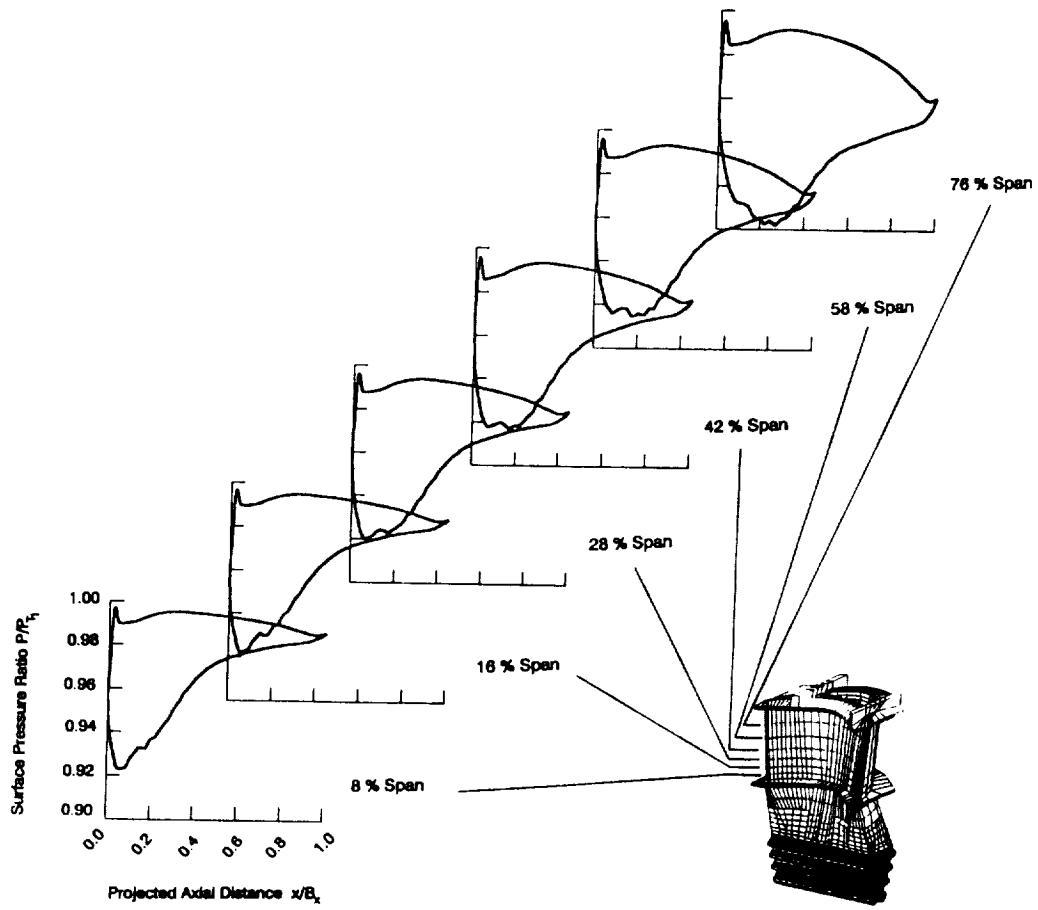


Figure 21. Turbine blade surface static pressure distributions

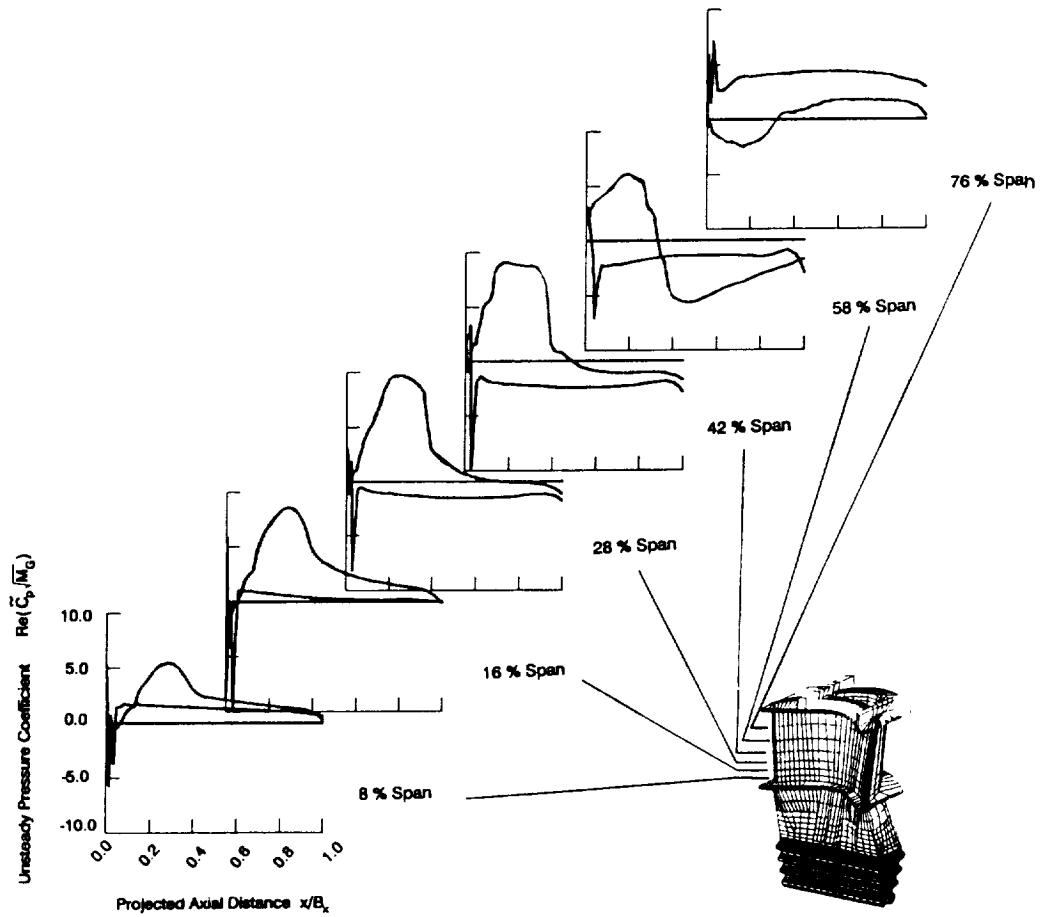


Figure 22. Turbine blade unsteady surface pressure distributions (real part) due to motion in second mode (edgewise)

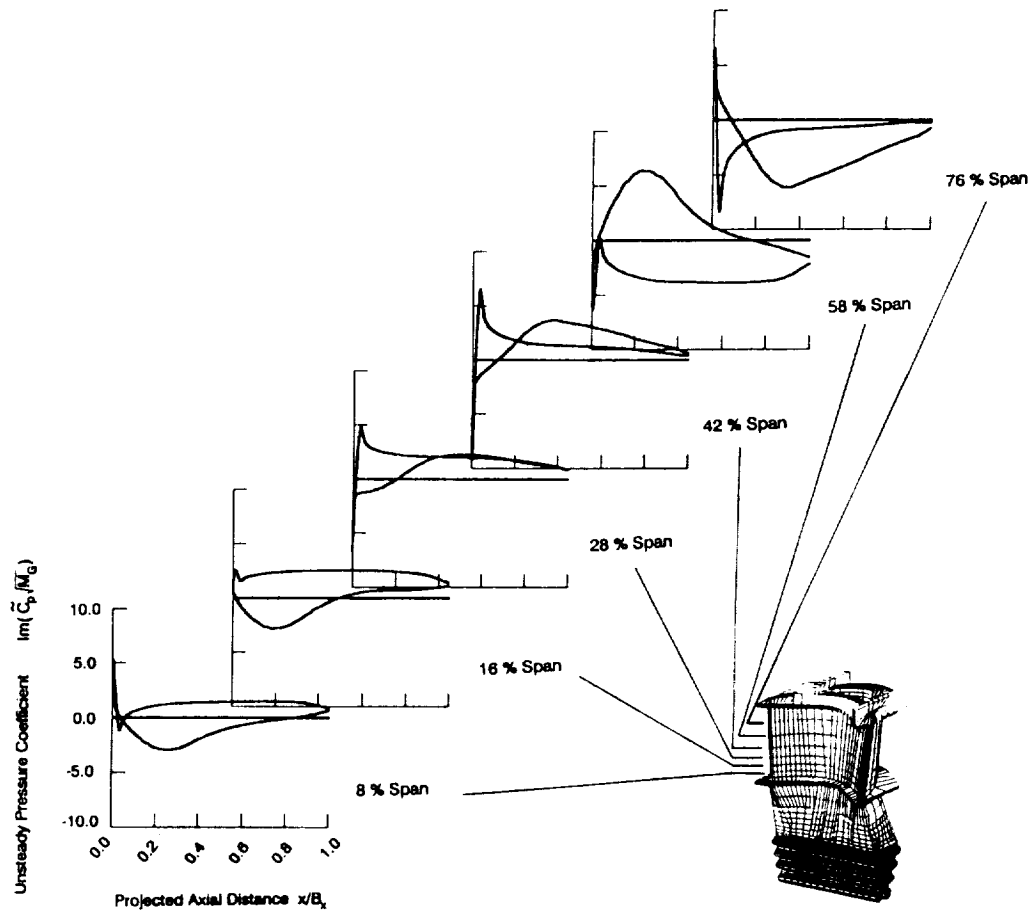


Figure 23. Turbine blade unsteady surface pressure distributions (imaginary part) due to motion in second mode (edgewise)

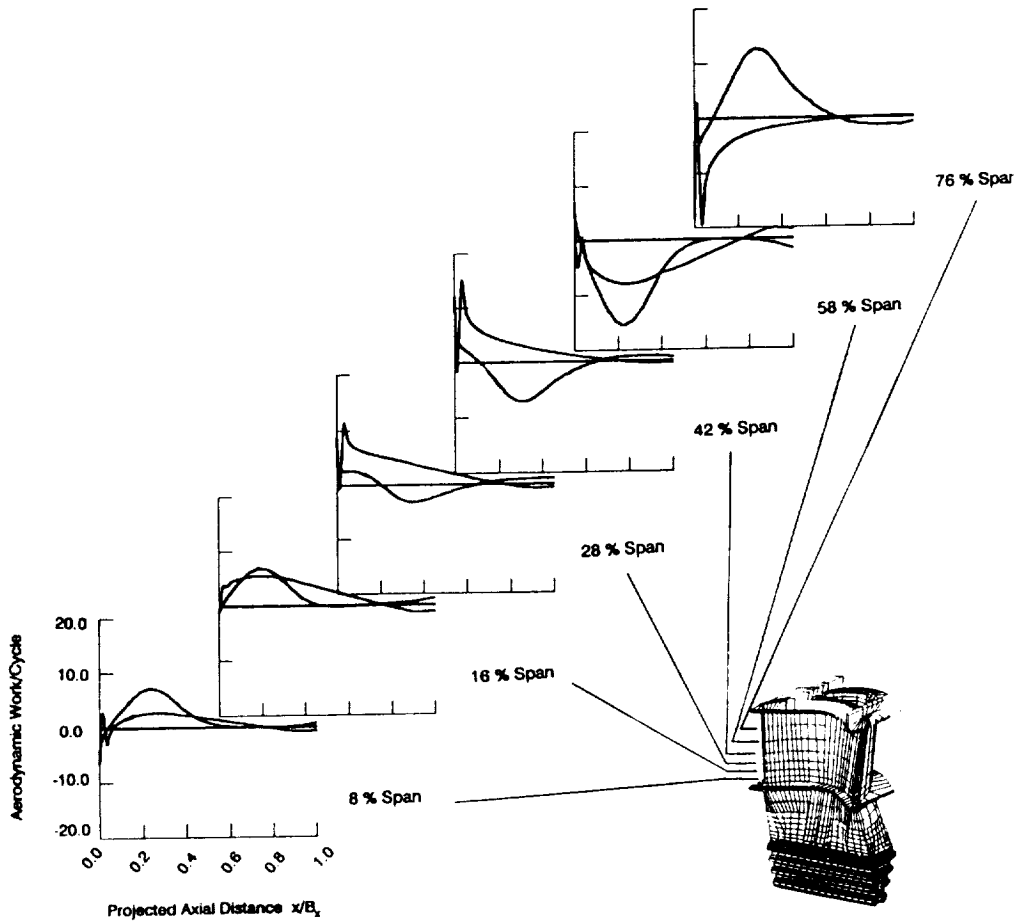


Figure 24. Turbine blade unsteady aerodynamic work per cycle distribution due to motion in second mode (edgewise)

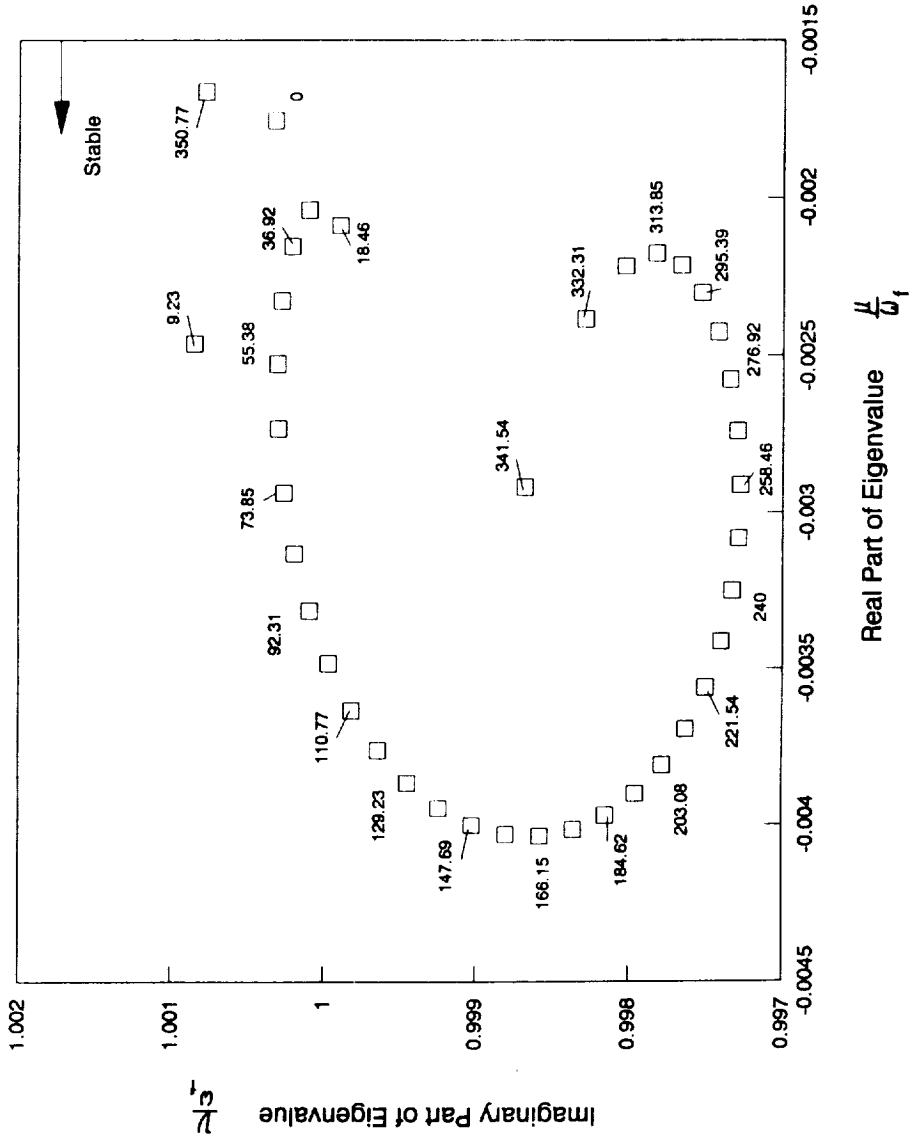


Figure 25. HPOTP turbine rotor tuned root locus for vibration in first mode (bending)

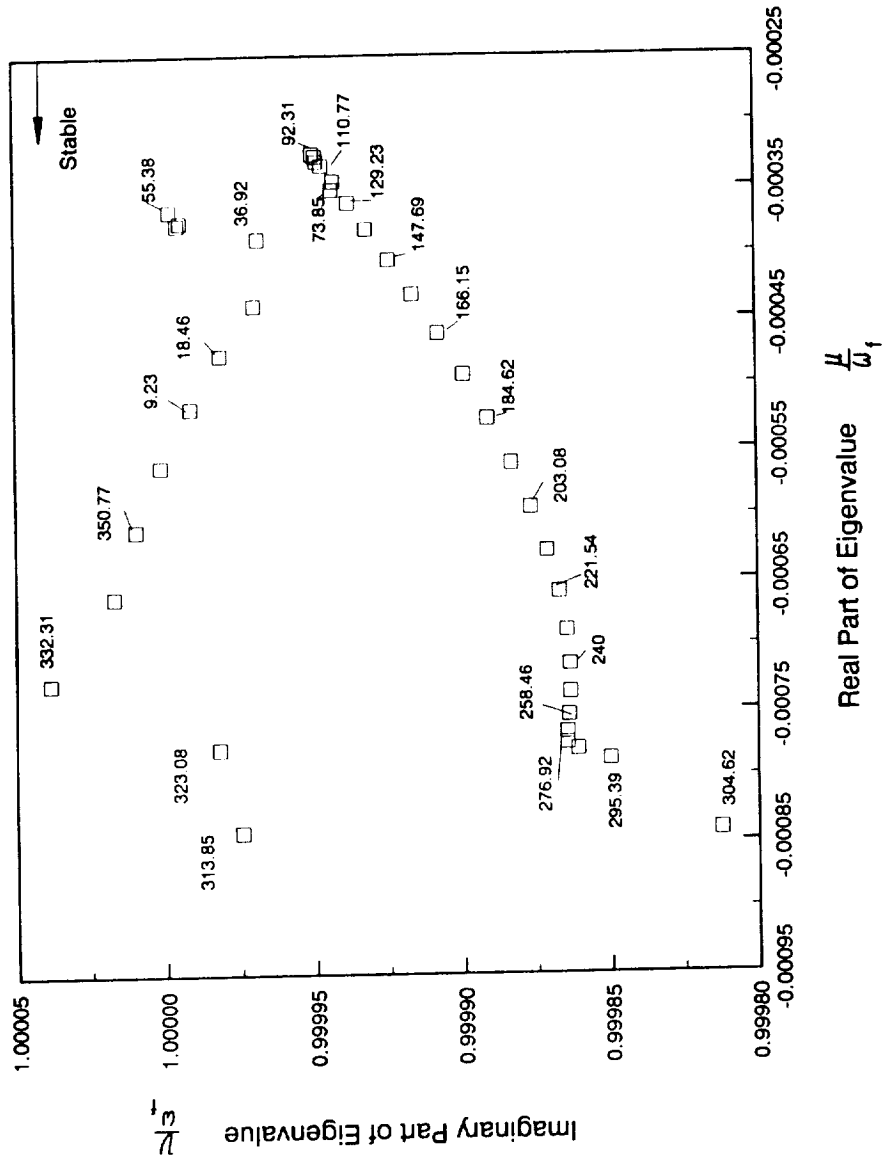


Figure 26. HPOTP turbine rotor tuned root locus for vibration in third mode (torsion), mechanical damping neglected

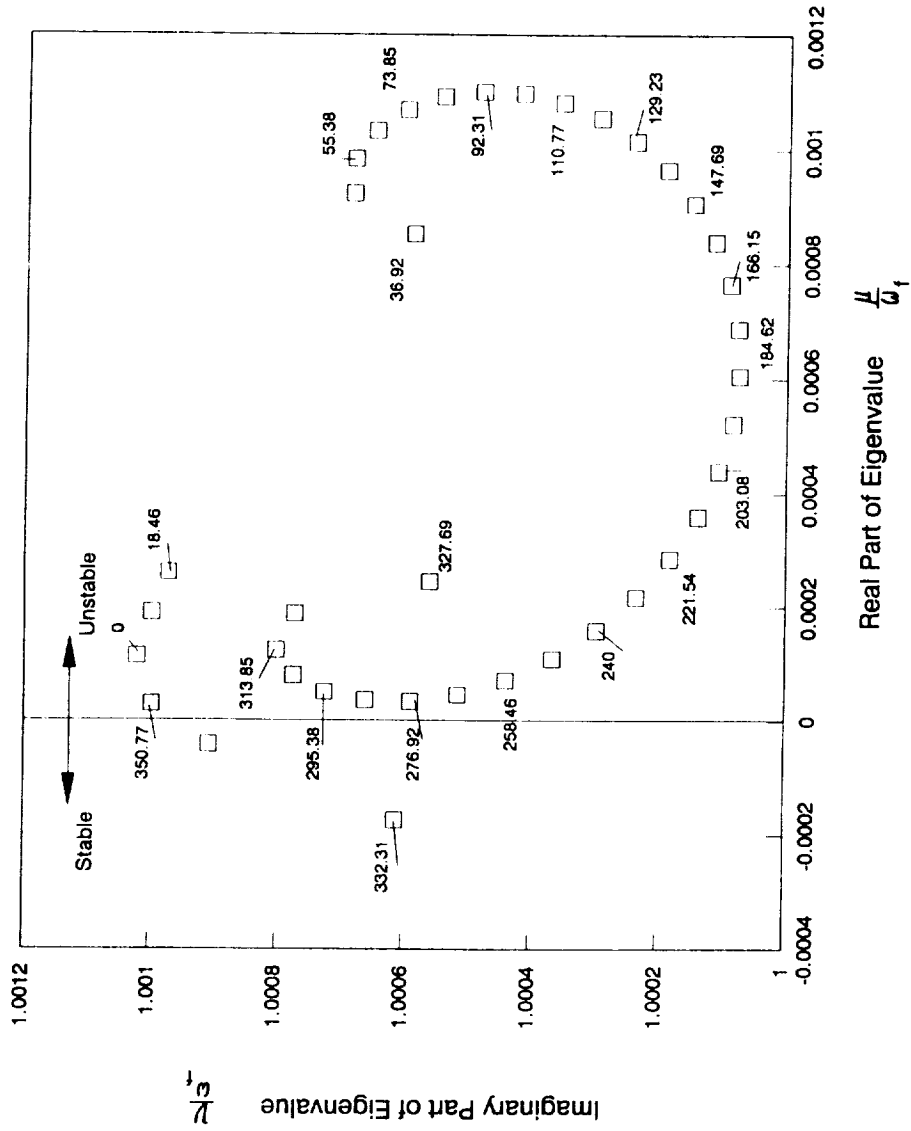


Figure 27. HPOTP turbine rotor tuned root locus for vibration in second mode (edgewise), mechanical damping neglected

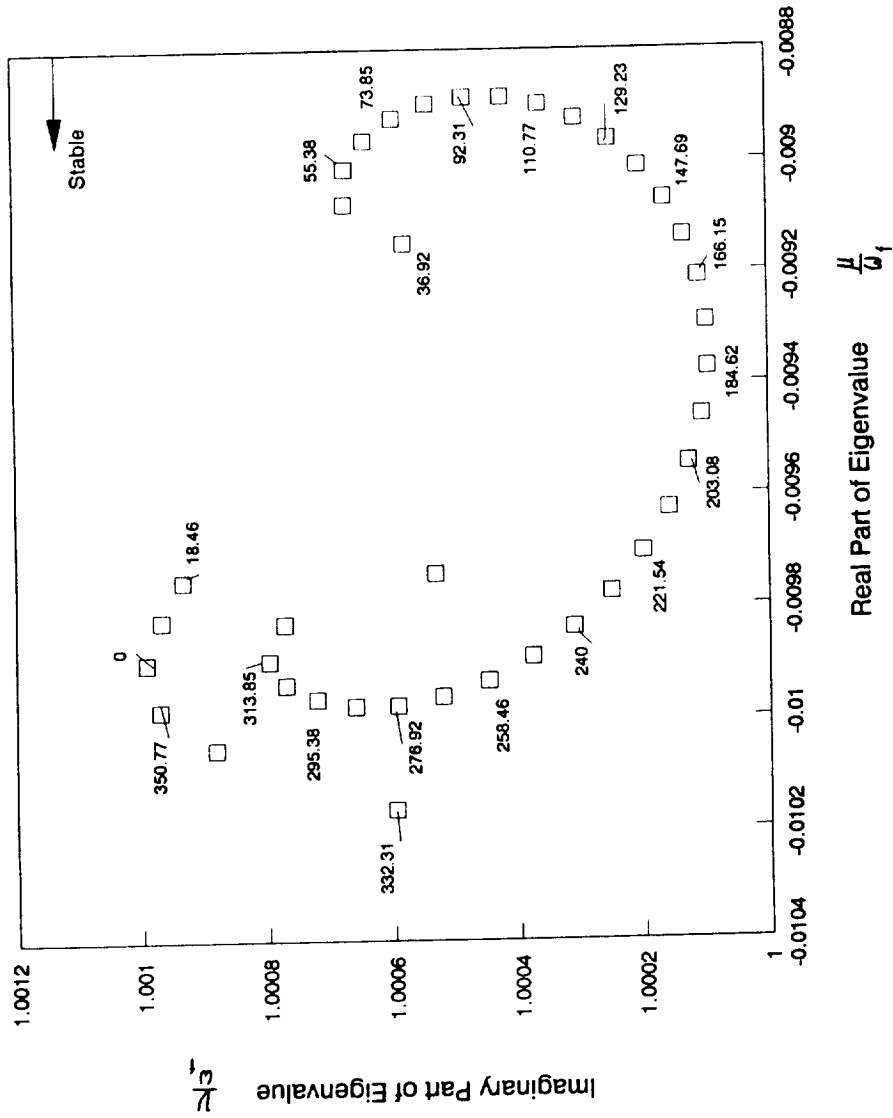


Figure 28. HPOTP turbine rotor tuned root locus for vibration in second mode (edgewise), 1.0% modal damping ratio included



National Aeronautics and  
Space Administration

## Report Documentation Page

1. Report No. NASA CR - 187089		2. Government Accession No.		3. Recipient's Catalog No.	
4. Title and Subtitle A Modal Aeroelastic Analysis Scheme for Turbomachinery Blading				5. Report Date March 1991	
				6. Performing Organization Code	
7. Author(s) Todd C. Smith				8. Performing Organization Report No. None (E - 6081)	
				10. Work Unit No. 505 - 63 - 1B	
9. Performing Organization Name and Address Sverdrup Technology, Inc. Lewis Research Center Group 2001 Aerospace Parkway Brook Park, Ohio 44142				11. Contract or Grant No. NAS3-25266	
				13. Type of Report and Period Covered Contractor Report Final	
12. Sponsoring Agency Name and Address National Aeronautics and Space Administration Lewis Research Center Cleveland, Ohio 44135 - 3191				14. Sponsoring Agency Code	
15. Supplementary Notes Project Manager, George L. Stefko, Structures Division, NASA Lewis Research Center. This report was submitted as a thesis in partial fulfillment of the requirements for the degree Master of Science in Mechanical Engineering to Case Western Reserve University, Cleveland, Ohio in January 1991.					
16. Abstract An aeroelastic analysis is developed which has general application to all types of axial-flow turbomachinery blades. The approach is based on linear modal analysis, where the blade's dynamic response is represented as a linear combination of contributions from each of its in-vacuum free vibrational modes. A compressible linearized unsteady potential theory is used to model the flow over the oscillating blades. The two-dimensional unsteady flow is evaluated along several stacked axisymmetric strips along the span of the airfoil. The unsteady pressures at the blade surface are integrated to result in the generalized force acting on the blade due to simple harmonic motions. The unsteady aerodynamic forces are coupled to the blade normal modes in the frequency domain using modal analysis. An iterative eigenvalue problem is solved to determine the stability of the blade when the unsteady aerodynamic forces are included in the analysis. The approach is demonstrated by applying it to a high-energy subsonic turbine blade from a rocket engine turbopump power turbine. The results indicate that this turbine could undergo flutter in an edgewise mode of vibration.					
17. Key Words (Suggested by Author(s)) Flutter; Turbomachinery; Aeroelasticity; Turbomachinery blades; Rotor blades (turbomachinery); Liquid propellant				18. Distribution Statement Unclassified - Unlimited Subject Category 07	
19. Security Classif. (of the report) Unclassified		20. Security Classif. (of this page) Unclassified		21. No. of pages 131	22. Price* A07



National Aeronautics and  
Space Administration

**Lewis Research Center**  
Cleveland, Ohio 44135

**Official Business**  
**Penalty for Private Use \$300**

**FOURTH CLASS MAIL**

**ADDRESS CORRECTION REQUESTED**



Postage and Fees Paid  
National Aeronautics and  
Space Administration  
NASA-451

**NASA**

---